



US Army Corps
of Engineers

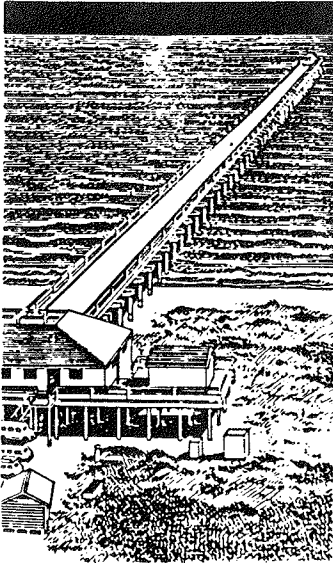
CONTRACT REPORT CERC-89-1

WAVE DISSIPATION ON A BARRED BEACH: A METHOD FOR DETERMINING SAND BAR MORPHOLOGY

by

Thomas C. Lippmann, Robert A. Holman

College of Oceanography
Oregon State University
Corvallis, Oregon 97331



September 1989

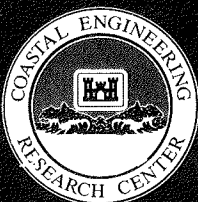
Final Report

Approved For Public Release; Distribution Unlimited

Prepared for DEPARTMENT OF THE ARMY
US Army Corps of Engineers
Washington, DC 20314-1000

Under Barrier Island Sedimentation Studies
Work Unit 31665

Monitored by Coastal Engineering Research Center
US Army Engineer Waterways Experiment Station
3909 Halls Ferry Road, Vicksburg, Mississippi 39180-6199



When this report is no longer needed return it to
the originator.

The findings in this report are not to be construed as an
official Department of the Army position unless so
designated by other authorized documents.

The contents of this report are not to be used for
advertising, publication, or promotional purposes.
Citation of trade names does not constitute an
official endorsement or approval of the use of such
commercial products.

REPORT DOCUMENTATION PAGE				Form Approved OMB No. 0704-0188	
1a. REPORT SECURITY CLASSIFICATION Unclassified		1b. RESTRICTIVE MARKINGS			
2a. SECURITY CLASSIFICATION AUTHORITY		3. DISTRIBUTION/AVAILABILITY OF REPORT Approved for public release; distribution unlimited			
2b. DECLASSIFICATION/DOWNGRADING SCHEDULE					
4. PERFORMING ORGANIZATION REPORT NUMBER(S)		5. MONITORING ORGANIZATION REPORT NUMBER(S) Contract Report CERC-89-1			
6a. NAME OF PERFORMING ORGANIZATION College of Oceanography Oregon State University		6b. OFFICE SYMBOL (If applicable)	7a. NAME OF MONITORING ORGANIZATION USAEWES, Coastal Engineering Research Center		
6c. ADDRESS (City, State, and ZIP Code) Corvallis, OR 97331		7b. ADDRESS (City, State, and ZIP Code) 3909 Halls Ferry Road Vicksburg, MS 39180-6199			
8a. NAME OF FUNDING/SPONSORING ORGANIZATION US Army Corps of Engineers		8b. OFFICE SYMBOL (If applicable)	9. PROCUREMENT INSTRUMENT IDENTIFICATION NUMBER		
8c. ADDRESS (City, State, and ZIP Code) Washington, DC 20314-1000		10. SOURCE OF FUNDING NUMBERS			
		PROGRAM ELEMENT NO.	PROJECT NO.	TASK NO.	WORK UNIT ACCESSION NO.
11. TITLE (Include Security Classification) Wave Dissipation on a Barred Beach: A Method for Determining Sand Bar Morphology					
12. PERSONAL AUTHOR(S)					
13a. TYPE OF REPORT Final report		13b. TIME COVERED FROM _____ TO _____	14. DATE OF REPORT (Year, Month, Day) September 1989		15. PAGE COUNT 58
16. SUPPLEMENTARY NOTATION Available from National Technical Information Service, 5285 Port Royal Road, Springfield, VA 22161.					
17. COSATI CODES			18. SUBJECT TERMS (Continue on reverse if necessary and identify by block number) See reverse.		
FIELD	GROUP	SUB-GROUP			
19. ABSTRACT (Continue on reverse if necessary and identify by block number) A technique is presented to remotely measure the scales and morphology of natural sand bars based on the preferential dissipation of wind waves and swell over the shallows of the bar. Images are recorded photographically or with video and statistical uncertainties associated with incident wave height modulations removed by averaging (time exposures). Ground-truth testing of the technique was carried out as part of the SUPERDUCK experiment in October 1986. The time exposures generally provided a good mapping of underlying morphology, allowing detection of the bar and determination of cross-shore and longshore length scales. However, during high waves, residual foam obscures the relationship of image intensity to local dissipation (modeled theoretically by dissipation of a random wave field), and an enhancement technique of image (Continued)					
20. DISTRIBUTION/AVAILABILITY OF ABSTRACT <input type="checkbox"/> UNCLASSIFIED/UNLIMITED <input type="checkbox"/> SAME AS RPT. <input type="checkbox"/> DTIC USERS			21. ABSTRACT SECURITY CLASSIFICATION Unclassified		
22a. NAME OF RESPONSIBLE INDIVIDUAL			22b. TELEPHONE (Include Area Code)		22c. OFFICE SYMBOL

Unclassified

SECURITY CLASSIFICATION OF THIS PAGE

18. SUBJECT TERMS (Continued).

Image time exposure

Photogrammetry

Sand bar morphology and scale

Superduck experiment

Video differencing

Wave breaking modeling

Wave shoaling

19. ABSTRACT (Continued).

differencing must be done to remove the bias of persistent form. Errors in bar location should be less than 35 percent, but this value depends on the geometry of the particular bar. Logistic simplicity and quantitative capabilities should make this technique very attractive.

Unclassified

SECURITY CLASSIFICATION OF THIS PAGE

PREFACE

This report is published to provide coastal engineers with a technique to remotely measure natural sand bar scale and morphology change. The work was prepared and published by the US Army Engineer Waterways Experiment Station (WES) with funds provided by Headquarters, US Army Corps of Engineers (HQUSACE), through the Barrier Island Sedimentation Studies Research Work Unit 31665 of the Shore Protection and Restoration Research Program. Technical Monitors were Messrs. John H. Lockhart and John G. Housley, HQUSACE.

Mr. Thomas C. Lippmann and Dr. Robert A. Holman of the College of Oceanography, Oregon State University, prepared this report under the direct supervision of Dr. Suzette M. Kimball, previous Chief of the Coastal Morphology Unit and Dr. Donald K. Stauble, present Chief of the Coastal Morphology Unit; and under general supervision of Mr. H. Lee Butler, Chief, Research Division, and Dr. James R. Houston and Mr. Charles C. Calhoun, Jr., Chief and Assistant Chief, Coastal Engineering Research Center (CERC), respectively.

Acknowledgment is extended to the entire Field Research Facility for their tireless efforts during SUPERDUCK, particularly Messrs. Curt Mason and Bill Birkemeier. Much credit and personal thanks is owed to Mr. Paul O'Neill, whose engineering skills and programming contributions made this work possible. Funding for the development of the image processing system and time exposure technique was provided by the Office of Naval Research, Coastal Sciences Program, under Contract No. N00014-84-0218. The ground-truth study during SUPERDUCK was funded by the US Army Corps of Engineers, CERC, under the Barrier Island Sedimentation Work Unit.

Commander and Director of WES during publication of this report was COL Larry B. Fulton, EN. Technical Director was Dr. Robert W. Whalin.

CONTENTS

PREFACE	1
LIST OF FIGURES	3
PART 1: INTRODUCTION	5
PART II: THEORY	8
Monochromatic Model	8
Random Wave Model	9
Application of the Models	11
Examples.	12
PART III: PHOTOGRAMMETRY	21
Theoretical Resolution and Accuracy	24
PART IV: FIELD TECHNIQUES	27
PART V: RESULTS.	34
Differencing Time Exposures	40
Shoreline Agreement	47
PART VI: DISCUSSION	50
PART VII: CONCLUSIONS.	52
REFERENCES.	53

LIST OF FIGURES

<u>No.</u>	<u>Page</u>
1 a. Oblique snap shot of wave breaking on October 10, 1987, at low tide during the SUPERDUCK experiment	7
1 b. A 10 minute time exposure from the same date and tide . .	7
2. Model results as waves are shoaled over a plane beach . .	13
3 Model test results for wave shoaling and dissipation over a surveyed profiled (top panel) from Torrey Pines beach on October 20, 1978	14
4 Model results for wave shoaling and dissipation over a barred beach profile from SUPERDUCK October 11, 1986. .	16
5 Influence of deep water rms wave height, H_0 , over a barred beach profile from SUPERDUCK October 11, 1986. .	17
6 Fractional error in locating the bar crest from theoretical dissipation maxima plotted against non-dimensional wave height, H^*_c	19
7 Geometry and labeling conventions used for photogrammetry	22
8 Map of the field site during the October portion of SUPERDUCK	28
9 Rectified time exposure image obtained at low tide on October 16, 1986, encompassing the minigrd area . . .	29
10 Example cross-shore intensity profile and bathymetry for October 16, 1986, during SUPERDUCK	30
11 Three-dimensional oblique views of the minigrd survey during SUPERDUCK	32
12 Bathymetry and cross-shore intensity profiles from a simple time exposure obtained at mid tide on October 6, 1986	35
13 Rectified time exposure image encompassing the minigrd area obtained at low tide on October 11, 1986	36
14 Location of the mean shoreline, measured bar crest, and intensity maxima from simple time exposures obtained at low, mid, and high tide on October 11, 1986	37
15 Shore-parallel transects centered over the mean bar distance 60 m and 70 m offshore	39

<u>No.</u>		<u>Page</u>
16	Rectified differencing time exposure obtained at low tide on October 12, 1986	41
17	Location of mean shoreline, measured bar crest, and intensity maxima from differenced time exposures obtained at low and mid tide on October 9, 1986	43
18	Local bathymetry and cross-shore intensity profiles from a differenced time exposure obtained at mid tide on October 9, 1986 for the three best-defined sand bar locations	44
19	Location of mean shoreline, measured bar crest, and intensity maxima from differenced time exposures obtained at low, mid, and high tide on October 11, 1986.	45
20	Location of mean shoreline, measured bar crest, and intensity maxima from differenced time exposures obtained at low, mid, and high tide October 16, 1986.	46
21	Results from differencing time exposures on October 9, 11-13, 15-16	48
22	All shoreline intensity maxima locations from simple time exposures.	49

TABLE

Table	Sampling Time, Wave Conditions and Video Quality Images Discussed in the Text	33
-------	---	----

WAVE DISSIPATION ON A BARRED BEACH: A METHOD FOR
DETERMINING SAND BAR MORPHOLOGY

PART I: INTRODUCTION

1. Offshore sand bars are common features of the world's coastlines. The amount of sediment associated with barred beaches makes them a very large and dynamic sediment transport region. While annual cycles in sediment deposition are observed on most coastlines (with offshore transport tending to form bars during higher energy wave conditions in winter months), significant morphological changes also occur on a much shorter time scale, especially in response to storms.

2. The many physical processes that contribute to the dynamics of barred beaches are not as simple as for plane beaches. Yet the new information available from studying these more complicated environments may provide valuable clues into the nature of fluid-sediment interactions. In particular, cross-shore and longshore length scales of bars may potentially be related to fluid parameters if appropriate dynamical models are available.

3. In fact, the literature contains a number of models of bar generation by fluid motions. It has been hypothesized that linear bars are formed at the breaker location of plunging incident waves (Keulegan 1948; Shepard 1950; Miller 1976), or perhaps under nodes or antinodes of waves standing against the shoreline (Carter et al. 1973; Lau and Travis 1973; Short 1975; Bowen 1980). Hypotheses also exist for the formation of three-dimensional crescentic (Bowen and Inman 1971), welded, and even apparently aperiodic sand bars, based for example, on the interaction of phase-locked edge waves (Holman and Bowen 1982). Yet, surprisingly, these models are largely untested under natural conditions.

4. There are several reasons why field tests have not been accomplished. Proper measurement of the low frequency surf beat invoked by several of the models, requires sophisticated analysis techniques to resolve particular trapped and leaky modes. Though this technique requires a more extensive array of instrumentation than originally thought, it is now at least feasible (Huntly et al. 1981; Oltman-Shay and Guza 1987).

5. Measuring the morphology over large enough spatial scales and short enough time scales remains a major difficulty, exacerbated by the scientific emphasis on storm periods when bar evolution is most rapidly occurring. Traditionally, bar measurements are made using in situ field techniques that, due to the roughness of the surf zone environment, are not always easily accomplished. Also, the large scale of most bar forms requires extensive surveying both cross-shore and alongshore, typically on the order of many hundreds of meters. Non-stationarity may lead to errors if the bar moves significantly during the surveying period. Hastening the surveying process can eliminate bar stationarity problems, but not without the inevitable loss in spatial resolution and the potential introduction of spatial aliasing.

6. We have developed a remote sensing technique that allows the visualization and subsequent quantification of nearshore morphology based on the patterns of incident wave breaking. However, instead of using an instantaneous image, we employ a long time exposure, thereby averaging out fluctuations due to incident wave modulations and giving a statistically stable image of the wave breaking pattern. Figure 1 illustrates the technique with an example. The breaking wave pattern in Figure 1 (a) suggests the presence of a sand bar, but the poor spatial coverage provided by breaking crests and the statistical uncertainty associated with the natural modulations in wave height render the details of the bar morphology uncertain. In Figure 1 (b), the breaking pattern has been averaged over a ten minute period in a time exposure. This image yields a much clearer view of the bar. Spatial coverage is both extensive and of high resolution. Non-stationarity problems are avoided since the sampling interval is only ten minutes, substantially less than the observed scaling time for appreciable bar movement (Sallenger et al. 1984). Finally, the logistics of the remote measurement technique are not constrained by surf zone roughness, and can be utilized wherever an adequate vantage point is accessible.

7. Our discussion of the technique will start with the theoretical background, followed by a section on the photogrammetry involved in the transformation of oblique images. The theoretical resolution and accuracy of the technique is then discussed, after which is a description of our field methods and laboratory digitization techniques using a computerized image processor. Finally, we will discuss field tests based on field data from the 1986 SUPERDUCK experiment (Crowson et al. in press).



Figure 1 a. Oblique snap shot of wave breaking on October 10, 1987, at low tide during the SUPERDUCK experiment.



Figure 1 b. A 10 minute time exposure from the same date and tide. The white band at the shoreline is the dissipation maximum corresponding to the shore break, while the bank offshore indicates the presence of a sand bar.

PART II: THEORY

8. The actual patterns of light intensity that are recorded as time exposure photographs are a result of the bubbles and foam of breaking waves. To relate this visible signal to the fluid motions (and hence the underlying bar morphology) we must make some assumptions about the mechanism of bubble formation. For the purposes of this paper, we will hypothesize that the light intensity recorded on the film, $I(x,y)$, is simply proportional to the local incident wave energy dissipation $\langle \epsilon(x,y) \rangle$,

$$I(x,y) \propto \langle \epsilon(x,y) \rangle \quad (1)$$

An analysis of dissipation over a barred profile should then indicate the capability of this technique to reveal underlying morphology.

9. We will consider two models of incident wave dissipation. The first is the depth-limited monochromatic model wherein the wave energy is represented by a single wave height, H_{rms} , and frequency, f . The second model is a random wave model where the wave energy is considered composed of a distribution of waves with heights that are described statistically. For both, we will approach the problem through the energy flux balance,

$$\frac{\partial}{\partial x} (Ec_g) = \frac{\partial}{\partial x} \left[\left(\frac{1}{8} \rho g H_{rms}^2 \right) c_g \right] = \langle \epsilon \rangle \quad (2)$$

where ρ is density, g is the acceleration due to gravity, E is the wave energy density, and c_g is the group velocity.

Monochromatic Model

10. The simplest representation of waves shoaling on a beach assumes that the incident energy is narrow-banded and can be represented by a single frequency and wave height. Outside the surf zone, dissipation is through bottom friction. This is small compared to surf zone breaking (Thornton and Guza 1983) and is of no interest for our application. Thus we take wave energy flux, Ec_g , to be conserved. Inside the surf zone, wave height is assumed depth-limited, similar to solitary wave theory (McCowan 1891) or monochromatic

lab results (Galvin and Eagleson 1965) and supported by field tests (Thornton and Guza 1982),

$$H_{rms} = \gamma h \quad , \quad x < x_b \quad (3)$$

where γ is a breaking constant (0.42 for this study), h is water depth, x is distance along the profile, and x_b is the offshore distance to the bar crest at mean tide. Thus wave energy flux is strictly a function of depth, and local dissipation is simply determined from the flux gradient (equation 2). Dissipation over an arbitrary beach profile can easily be calculated using (2) and (3).

11. The monochromatic model, while simple, has several distinct disadvantages. First, if taken strictly, wave heights should actually increase as waves propagate over a sand bar and into the deeper water of the trough. However, this non-physical result can be simply avoided if, as a wave is numerically shoaled, the criterion for whether it is breaking is based on a "local" wave height, calculated by inviscid shoaling from the point immediately offshore. The second problem will generally be at the initial break point. This is, again, a non-physical result, as well as an unfortunate one for our technique since we are interested in using the intensity signal to determine the location of the bar crest, not the break point. However, this problem, which also occurs in the theory of longshore currents, can be corrected by considering a random wave model for incident wave heights (Thornton and Guza 1983).

Random Wave Model

12. Models for the shoaling and breaking of random wave fields have been published by a number of authors (Collins 1970; Battjes 1972; Kuo and Kuo 1974; Goda 1975; Battjes and Janssen 1978; Thornton and Guza 1983). These consider the wave energy to be composed of a distribution of waves of varying height. The analysis is then carried out statistically, representing the waves in terms of probability distributions whose bulk properties may be found by integration. Many of these models still invoke depth-limited breaking with

dissipation being determined from equation (2) as the gradient of a depth-limited flux. However, the latter two (Battjes and Janssen 1978, Thornton and Guza 1983) instead, specify dissipation and use (2) in the opposite direction to find wave height. Our analysis will follow this procedure.

13. Using the extensive data set from the Nearshore Sediment Transport Study (NSTS), Thornton and Guza (1983) showed that the wave heights, H , of a random incident wave field were well described by a Rayleigh probability distribution,

$$p(H) = \frac{2H}{H_{rms}^2} \exp\left[-\left(\frac{H}{H_{rms}}\right)^2\right] \quad (4)$$

Surprisingly, this result was found to be valid throughout the entire near-shore region including the surf zone where the underlying assumptions of linearity are clearly violated.

14. As the wave field shoals, some portion of the waves begin to break, modifying the distribution. The form of this modification is the main distinguishing feature of the above-listed references. Thornton and Guza (1983) are unique in that their model for the shoaling of the wave height distribution is based on field data from a barred beach (Soldier's Beach, California) wherein the wave height time series were augmented with a record of waves which were actually breaking. They express the probability distribution of breaking waves, $p_b(H)$, as a weighting of the distribution of all waves,

$$p_b(H) = W(H) p(H) \quad (5)$$

where, from the data, they determine the best form of the weighting function to be

$$W(H) = \left(\frac{H_{rms}}{\gamma h}\right)^2 \left\{ 1 - \exp\left(-\left(\frac{H}{\gamma h}\right)^2\right) \right\} \quad (6)$$

They then model the dissipation of a breaking wave based on a periodic bore model (Stoker 1957; Hwang and Divoky 1970),

$$\epsilon = \frac{f}{4} \rho g \frac{(BH)^3}{h} \quad (7)$$

where B is empirical breaker coefficient, roughly representing the fraction of the bore face that is covered with foam. The mean dissipation, $\langle \epsilon \rangle$, is then just the integral through the wave height distribution,

$$\langle \epsilon \rangle = \frac{3\sqrt{\pi}}{16} \rho g B^3 f \frac{H_{rms}^5}{\gamma^2 h^3} \left[1 - \frac{1}{\left(1 + \left(\frac{H_{rms}}{\gamma h}\right)^2\right)^{5/2}} \right] \quad (8)$$

Application of the Models

15. Numerical implementation of the two models was carried out to determine the behavior of dissipation over profiles in general, and to provide a comparison for field tests, to be discussed later in the paper. The energy flux balance, equation 2, forms the basis of the model. Thornton and Guza 1983 note that in testing a variety of numerical schemes, the simplest forward stepping technique was found to be sufficiently accurate. We will use this same algorithm,

$$Ec_g \Big|_2 = Ec_g \Big|_1 + \langle \epsilon \rangle \Big|_1 \Delta x \quad (9)$$

Starting from the deepest grid point (assuming a wave height that has been linearly shoaled from deep water), the wave energy flux is stepped landward. For the random wave model, the flux at any shoreward point, labelled 2, is calculated using the flux and dissipation (equation 8) found at the next seaward point, labelled 1. For the monochromatic model, the rms wave height at each point, 2, is taken as the smaller of γh_2 or $H_1(h_1/h_2)^{1/4}$, and $\langle \epsilon \rangle$ found from (9). Note that the shallow water assumption is valid for all cases examined. Values used for B and γ are 1.54 and 0.42 respectively, taken as representative of field data (Thornton and Guza 1983).

Examples

16. Theoretical dissipation profiles have been calculated for three beach profiles. The first, a plane beach, provides a good illustration of the differences between the monochromatic and random wave models. The second, Torrey Pines beach (the site of the NSTS) was used first to check the model results against Thornton and Guza (1983) as an error check of the programming and secondly to show the sensitivity of dissipation to minor perturbations in an otherwise simple profile. Finally, a barred profile from the SUPERDUCK experiment was used to show the ability of dissipation (and hence the time exposure technique) to highlight the bar crest location. The latter case was also used to provide an understanding of the ground truth studies, conducted during SUPERDUCK, that will be discussed later.

17. Figure 2 shows the behavior of the two models on a plane beach profile, shown in the top panel. The monochromatic model, shown in the middle panel behaves as expected, with energy flux conserved (zero dissipation) until the local H_{rms} exceeds γh when dissipation is suddenly a maximum (but for the one intermediate point which arises artificially due to finite step size). On the other hand, the random wave model shows a much broader maximum, recognizing the distribution of breakers with some dissipation arising offshore from the occasional energetic wave while nearly all waves are breaking near the shoreline, but are of low energy. There is a dissipation maximum despite the fact that the beach profile is plane. Interestingly, the location of maximum dissipation is the same for both models. The area under both curves is also the same, and must equal the deep water energy flux.

18. Figure 3 shows the model results for Torrey Pines beach on 10/20/78, during the NSTS experiment. This day was chosen as one of the two data runs analyzed in Thornton and Guza (1983) against which we could check the functioning of our model. Again, the beach profile is shown in the top panel, with associated H_{rms} and $\langle \epsilon \rangle$ curves for the monochromatic and random wave models shown in the middle and lower panels, respectively. One of the problems of the monochromatic model is immediately apparent. The dissipation curve shows an extreme artificial sensitivity to details of the beach profile, in contrast to the more physically sensible behavior of the random wave model. Figure 3 also illustrates a second difference between the two models. For the particular wave height used, the waves are barely starting to break over the

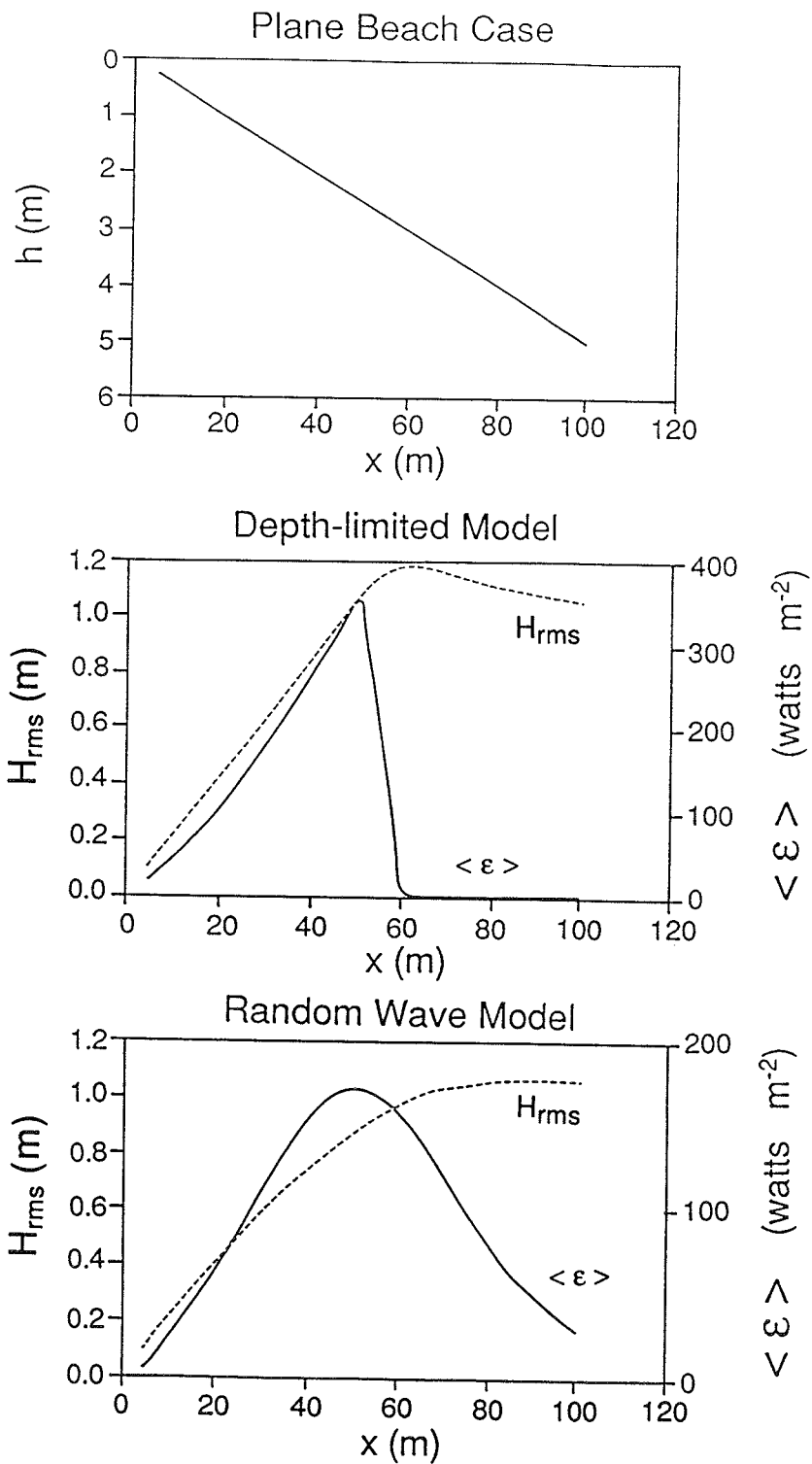


Figure 2. Model results as waves are shoaled over a plane beach profile (top panel). The behavior of H_{rms} and $\langle \epsilon \rangle$, plotted against offshore distance, is shown for the depth-limited monochromatic model in the middle panel and for the random wave model in the bottom panel.

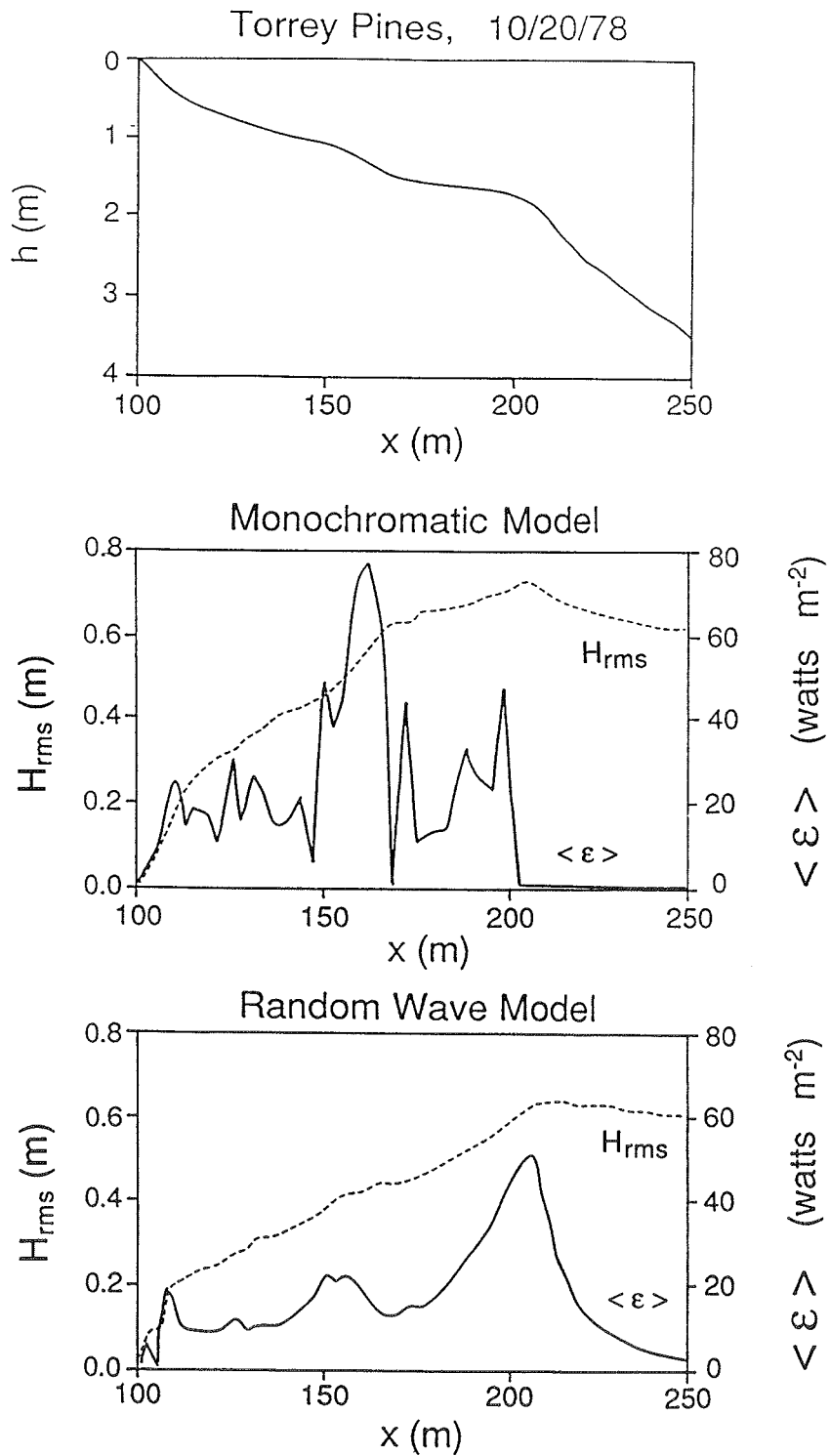


Figure 3. Model test results for wave shoaling and dissipation over a surveyed profiled (top panel) from Torrey Pines beach on October 20, 1978. The cross-shore behavior of H_{rms} and $\langle \epsilon \rangle$ are shown for the monochromatic model in the middle panel and for the random wave model in the lower panel

offshore bump ($x=200$ m) if the wave field is considered monochromatic. Thus the local dissipation peak is poorly defined. By contrast, the random wave model yields a well-defined peak, a result of allowing a distribution of wave heights.

19. It appears from Figure 3 that the imaging of dissipation may prove very helpful in determining the horizontal length scales of perturbations (sand bars, terraces) to a beach profile. Since the magnitude of dissipation is dependent on beach slope, peaks of dissipation will reflect positive changes of slope ("bumps" in the perturbation profile).

20. Figure 4 shows wave shoaling and dissipation for a barred beach profile (a linear storm bar that formed during the SUPERDUCK experiment). A second perturbation 375 m offshore is the residual of a semi-permanent second linear bar. Three features are apparent in the dissipation curves. Offshore, the presence of the second bar (perturbation) is indicated on the random wave curve by a small dissipation peak, shoreward of which dissipation is lower but not zero. This is similar to the results for the low-tide terrace on Torrey Pines beach. Note that the monochromatic model completely misses this feature. The well-developed inner bar is clearly highlighted by the dissipation curves for both models. However, the location of maximum dissipation is displaced seaward from the measured bar crest (location of minimum depth) by 20 m for the random wave field and 40 m for monochromatic waves, a result of weighting the dissipation toward the larger waves. Continuing landward, the trough is indicated by a region of essentially zero dissipation. This contrast between the large dissipation over the bar and zero over the trough distinguishes (at least qualitatively) the signal due to sand bar morphology from that of a terrace or more minor perturbation. Finally, we see a narrow dissipation maximum near the shoreline, a feature that also shows up in the field tests discussed later. While the presence of this "shorebreak" maximum is reasonable, the details of its location may be poorly reproduced since our dissipation models artificially force wave height to zero at the shoreline (we allow no standing wave component).

21. The influence of deep-water wave height, H_0 is shown in Figure 5. For any offshore position, it appears that an increase in H_0 will result in an increase in local wave height, H_{rms} , up to a maximum value which depends on depth. Further increases in H_0 have no effect and the local wave field is said to saturate. This behavior shows the merging of the dissipation-based

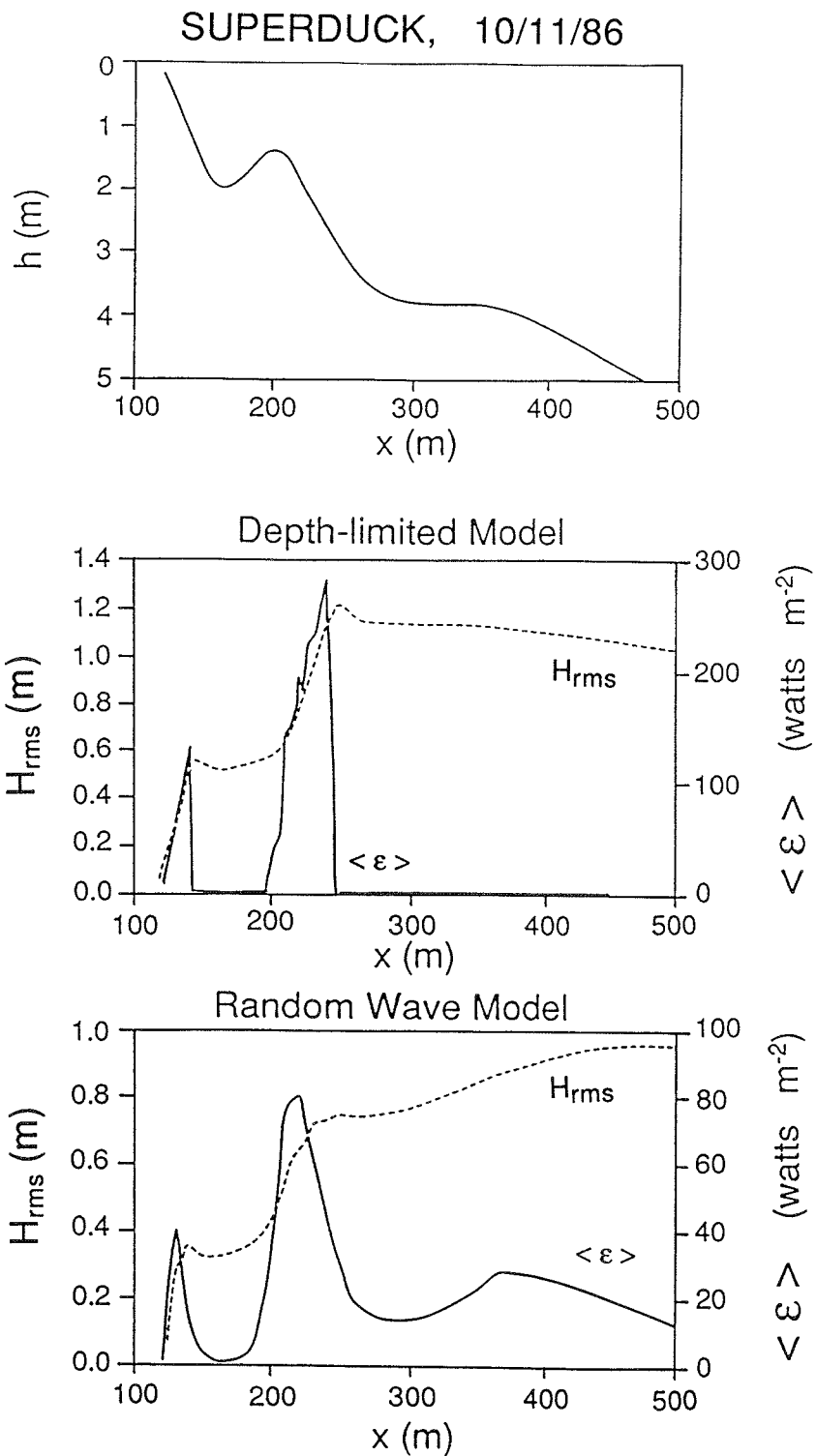


Figure 4. Model results for wave shoaling and dissipation over a barred beach profile (top panel) from SUPERDUCK on October 11, 1986. The cross-shore behavior of H_{rms} and $\langle \epsilon \rangle$ are shown for the monochromatic model in the middle panel and for the random wave model in the lower panel.

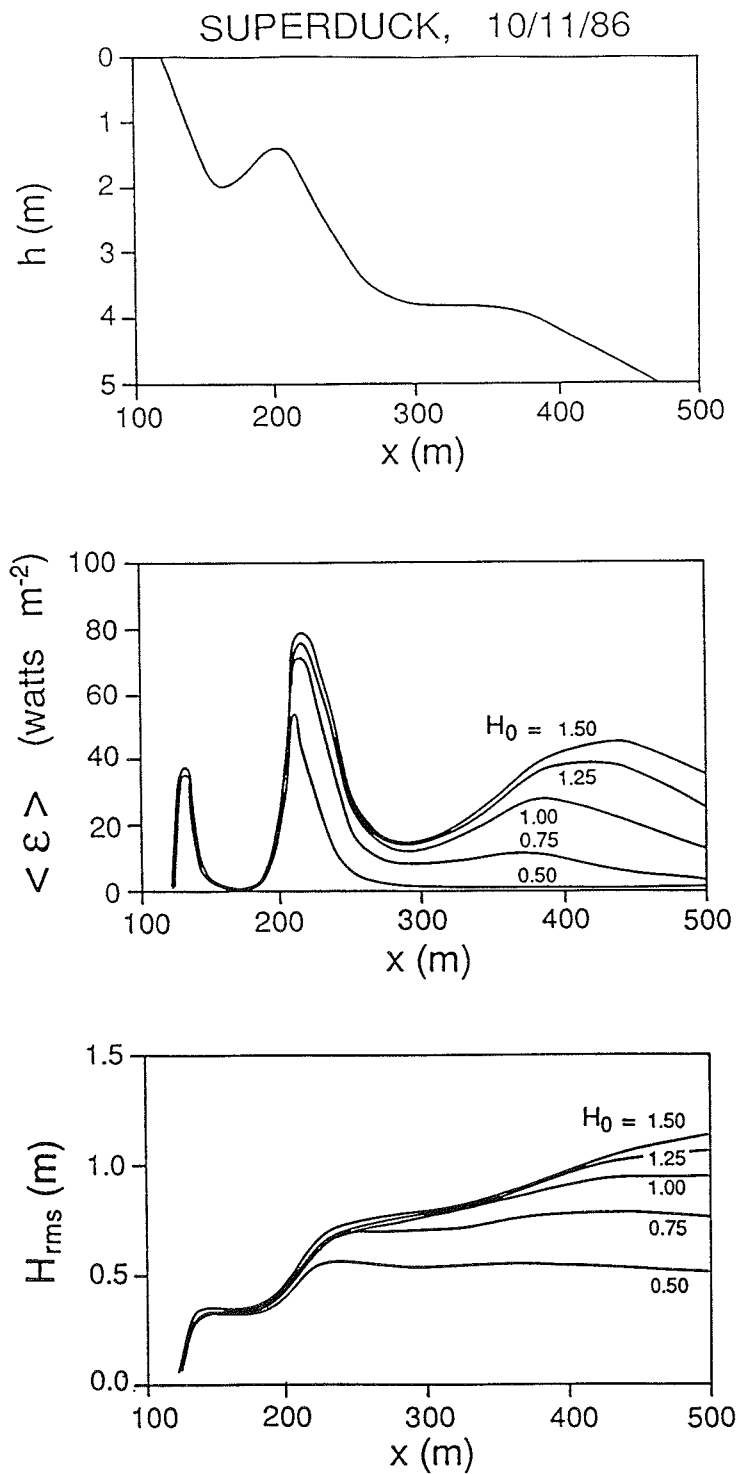


Figure 5. Influence of deep water rms wave height, H_0 , over a barred beach profile (top panel) from SUPERDUCK on October 11, 1986. The effect of increasing H_0 on dissipation, $\langle \epsilon \rangle$, and local wave height, H_{rms} , at offshore locations are shown in the middle and lower panels, respectively

model of shoaling used here with earlier depth-limited models for depths that are "shallow" with respect to the wave height, a point that was also made theoretically in Thornton and Guza 1983.

22. Variation of wave period, T , will affect the model in two ways. The deep water energy flux (hence area under the dissipation curve) depends linearly on T . Also, dissipation (equation 8) is just inversely proportional to T . The net result is that dissipation profiles for different wave periods have different magnitudes but the same structure, including location and shape of peaks.

23. The saturation behavior of dissipation is beneficial to our objective of locating sand bar features since the location of the dissipation maximum is only weakly sensitive to offshore wave parameters. This is quantified in Figure 6 which shows the fractional error in locating the bar crest (difference between the location of the dissipation maximum and the measured bar crest position, Δx , divided by the offshore distance to the bar crest at mean tide, x_b) versus the non-dimensional wave height,

$$H_c^* = \left(\frac{H_0}{\gamma h_c} \right) \left(\frac{k_c}{2k_0} \right)^{\frac{1}{2}} \quad (10)$$

The variables h_c and k_c refer to the depth and local wave number at the bar crest, and H_c^* is similar in form to equation (3), but with a wave height that would result from linear shoaling from deep water. Figure 6 shows that the fractional error in locating the bar crest varies from 0 percent for small waves that just break over the bar ($H_c^* = 0.5-1.0$) to about 35 percent for a saturated wave field.

24. The above analysis suggests that if the visible intensity signal recorded in time exposure photographs does depend on incident wave dissipation, then the time exposure technique should work. Best results will occur for waves which just break over the bar, but even for larger waves, the error in bar location identification will reach a maximum value, 35 percent for the above case. If the results are to be used to test bar generation models based on standing wave motions, wherein the bar location scales as

SUPERDUCK; 11 OCT 87

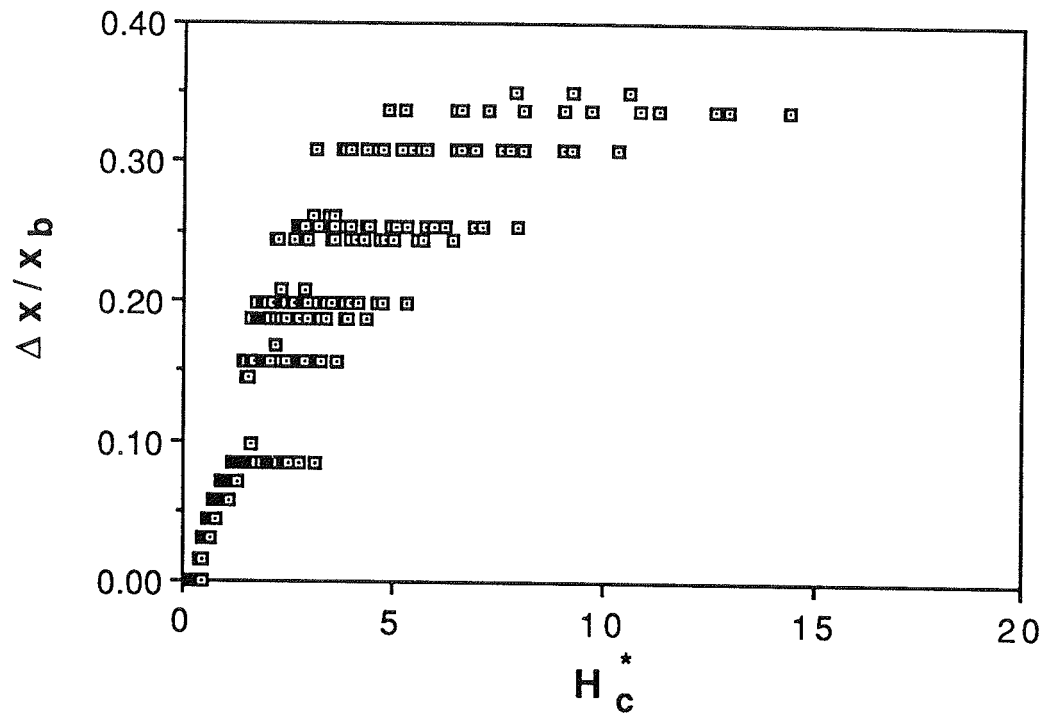


Figure 6. Fractional error in locating the bar crest from theoretical dissipation maxima plotted against non-dimensional wave height, H_c^*

$$\lambda = \frac{f^2 x}{g\beta} \quad (11)$$

where β is the effective beach slope, then errors of less than 18 percent will occur in the predicted frequency, f , of the standing wave. It should be noted that this value is just from one sample geometry and would be different for different beach profiles. For instance, the value of x_b does not enter into the dimensional error, Δx , so that for bars that are farther offshore the error would be smaller, and visa-versa. Similarly, at higher tide, H_c^* would be smaller (due to larger h_c) and x_b would be larger. Both would tend to yield smaller relative errors. Again, the opposite is also true, so that low tide estimates will tend to be worse.

PART III: PHOTOGRAMMETRY

25. Oblique images were used to quantify the offshore length scales of the sand bar (and potentially other variables). The location of any object in the image is a function of the spatial orientation of the camera in relation to ground topography, and can be determined by a simple analysis of the geometry. We will outline the equations that define the transformation between image coordinates and ground coordinates. When transforming from ground to image coordinates, the equations are fully defined. However, since the image is two-dimensional while the ground is three-dimensional, the opposite process (called rectification) is underdetermined. We overcome this by assuming one dimension to be known. For example, in rectifying images of waves, we assume the vertical coordinate to be at sea level and that errors of the order of the wave amplitude are negligible compared to the height of the camera.

26. The geometry and labeling conventions used in the rectification process are shown in Figure 7. The optic center of the camera is located at point O, a distance Z_c above the ground plane. The camera nadir line intersects the ground at the nadir, N. The image points lie in the focal plane, which for our purposes will be considered the 1:1 positive, consistent with traditional photogrammetry conventions. The focal plane is separated from O by the focal length, f_c , called the principal point, and forms an angle τ (the camera tilt) with the vertical nadir line. The principal line passes through the principal point and bisects the focal plane. The principal point is also the origin for the image coordinate system with the principal line as the y-axis. The nadir point acts as the origin for the camera coordinate system with the principal line in the ground plane defining the positive Y-axis. Image coordinates will be denoted with small letters, (x,y), and ground coordinates will be denoted with capital letters, (X,Y).

27. The ground location of any point, Q, is determined from its image coordinates (x_q, y_q) by

$$\begin{aligned} X_Q &= Z_c \sec(\tau + \alpha) \tan \gamma \\ \text{and} & \\ Y_Q &= Z_c \tan(\tau + \alpha) \end{aligned} \tag{12}$$

where the angles α and γ are defined by the location of image points as

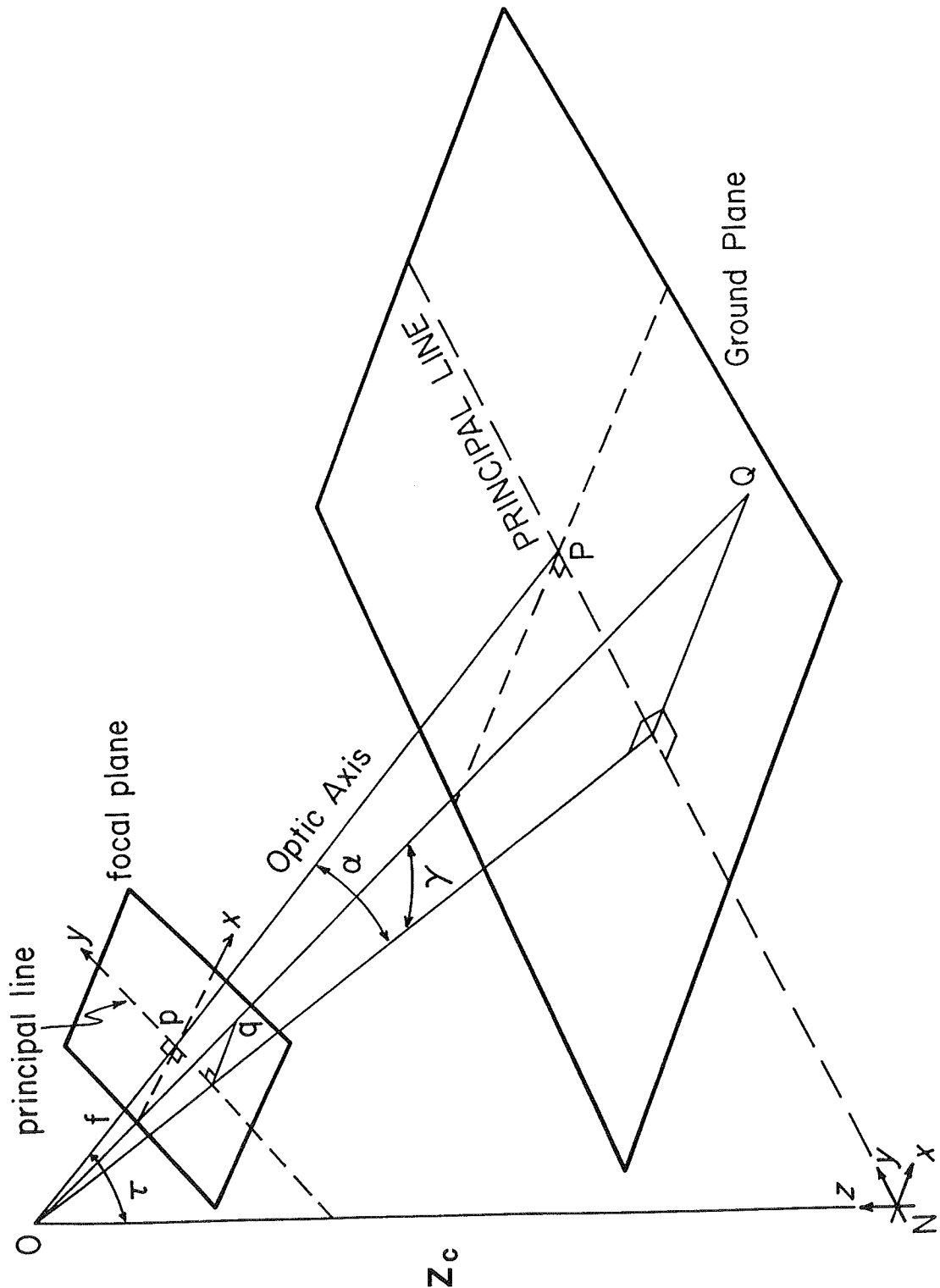


Figure 7. Geometry and labeling conventions used for photogrammetry

$$\alpha = \tan^{-1} \left(\frac{y_q}{f_c} \right)$$

and

$$\gamma = \tan^{-1} \left(\frac{x_q}{\sqrt{y_q^2 + f_c^2}} \right)$$

(13)

Transformation in the opposite direction, from ground to image points, is done by simply inverting and combining (12) and (13) to yield

$$y_q = f_c \tan \left(\tan^{-1} \left(\frac{Y_Q}{Z_c} \right) - \tau \right)$$

and

$$x_q = \left(\frac{y_q^2 + f_c^2}{Z_c^2 + Y_Q^2} \right)^{1/2} X_Q$$

(14)

28. Several complications arise in applying these relationships in the field. First, these equations are a function of the camera tilt and focal length. However, field measurement of tilt may be awkward and inaccurate, and the focal length of a zoom lens may be hard to estimate. Second, we do not generally work from a 1:1 positive, but instead either read distances on a photographic enlargement or count picture elements (pixels) on a television screen. In doing so, we will have altered the apparent focal length of the image by an unknown amount. We can solve for the "magnified" focal length analytically using

$$f'_c = \frac{x_e}{\tan^{-1} \frac{\delta}{2}} \quad (15)$$

where x_e is the measured distance from the principal point to the right hand edge of the enlarged image, and δ is the horizontal field of view of the lens. Unfortunately, for most cases, δ itself is not accurately known. Third, the direction of aim of a camera in the field is generally chosen to give the best view. Thus, the ground coordinate system defined by the principal line may not be particularly convenient. The transformed ground points can be easily rotated into a more traditional coordinate system, for example

with the x-axis directed offshore, if the angle, ϕ between the two coordinate systems is known. Unfortunately, accurate estimation of ϕ in the field is again difficult.

29. The unknowns, f_c , τ and ϕ can be determined quite accurately by making use of targets at known locations in the image. By knowing both the ground and image coordinates of particular points, equations (12), (13), and (14) can be solved iteratively to calculate the unknowns. If two or more known points are used, the problem is over-determined and can be solved by minimizing an appropriate error term. Using this technique in analyzing the images discussed later in the paper, we find typical errors in the estimates of τ , ϕ and f_c to be less than 0.25 deg, 0.5 deg, and 0.5 percent respectively, roughly consistent with theoretical expectations discussed below.

Theoretical Resolution and Accuracy

30. The photogrammetric measurements outlined in the last section are based on estimates of one distance (the camera height) and two angles (vertical and azimuthal). The precision of the technique then relies on the precision of each of these estimates.

31. While there may be errors associated with estimating camera height above some surface, there is no inherent limitation on that measurement. On the contrary, there is a discrete resolution associated with our estimates of angle. For image quantification, we use an image processing system (described later) which breaks the image into a 512 x 512 array of pixels. Since we can resolve to no better than $\pm 1/2$ pixel, we find a fundamental limit on angular resolution to be $\Delta\alpha = \Delta\gamma = \delta / 1024$ (assuming $\tan \delta/2 \approx \delta/2$). For our typical wide angle lens, $\delta = 40^\circ$, so $\Delta\alpha = 0.04^\circ = 7 \times 10^{-4}$ radians.

32. From equation (12), we see that the precision of estimates in Y_Q is given by

$$\frac{\Delta Y_Q}{Y_Q} = \frac{\Delta H_c}{H_c} + \frac{2\Delta(\tau+\alpha)}{\sin 2(\tau+\alpha)} = \frac{2\Delta(\tau+\alpha)}{\sin 2(\tau+\alpha)} = \frac{1.4 \times 10^{-3}}{\sin 2(\tau+\alpha)} \quad (16)$$

Sensibly, resolution degrades as $(\tau + \alpha)$ approaches $\pi/2$, or as the point of view approaches the horizon. If we take the maximum useful vertical angle to be 85 deg (5 deg from the horizon), the resolution in Y will be 0.8 percent. Note that the fractional errors also increase as the view approaches nadir.

However, this is simply a function of normalizing by Y , which goes to zero at the nadir; absolute errors will actually be a minimum.

33. The error in X estimates (normalized by Y_Q , roughly representing the distance from the camera) is given by

$$\frac{\Delta X_Q}{Y_Q} = \left(\frac{\Delta H_c}{H_c} \right) \frac{\tan \gamma}{\sin(\tau + \alpha)} + \frac{\tan \gamma \Delta(\tau + \alpha)}{\cos(\tau + \alpha)} + \frac{1}{\sin(\tau + \alpha)} \frac{\Delta \gamma}{\cos 2\gamma} \quad (17)$$

For typical camera views, $\sin(\tau + \alpha) \approx 1$, hence the theoretical resolution is again limited by angular resolution through the last two terms. Using representative values, we find a worst case resolution of 0.3 percent, a smaller value than for Y , partly due to the choice of normalization. Since the camera coordinate system is not usually aligned with the survey system, we chose a conservative estimate that spatial resolution in either axis will be on the order of 0.8 percent of the distance from the camera.

34. While fundamental limits on precision depend, for our system, simply on the angular size of the pixels, the absolute accuracy of our measurement depends on cumulative errors from a number of estimates. If the location of the camera is well known, the error in the first term of (16) and (17) results largely from errors in determining sea level (assuming that the ocean surface is being imaged). For the data discussed later, this will be on the order ± 0.25 m with a camera height on 40 m, so that the relative error contribution is 0.65 percent. This error could be substantially larger for lower camera heights. Estimation of the vertical and horizontal angles actually incorporates parameters such as τ , f and ϕ , each of which has associated errors. If we assume that the parameters themselves were estimated based on the location of two known points (as outlined in the previous discussion), then they will collectively incorporate the error of four separate angle measures, $4\Delta\alpha$. Including the error associated with estimating the angle of interest, the total angular error could be $5\Delta\alpha = 0.20^\circ = 3.5 \times 10^{-3}$ radians. For a maximum vertical angle of 85 deg, and including the error for camera height, the theoretical worst case accuracy should be

$$\frac{\Delta X_Q}{Y_Q} < \frac{\Delta Y_Q}{Y_Q} = 0.65\% + (5 \times 0.8\%) < 5\% \quad (18)$$

35. As shown, the accuracy and resolution of the system depend on the angular field of view, δ , and the vertical angle, $(\tau + \alpha)$. The value of δ used here is for a wide angle lens and gives a worst case result. Clearly, a telephoto lens, zoomed in on the subject at hand, will yield improved estimates. The vertical angle becomes critical as $(\tau + \alpha)$ approaches the horizon. While 85 deg is a reasonable value for a maximum angle, a better approach to experimental design would be to determine the required resolution and camera geometry, then solve for the maximum vertical angle for which this resolution is achievable.

PART IV: FIELD TECHNIQUES

36. The time exposure technique for measuring large scale nearshore morphology was tested as part of the DUCK85 and SUPERDUCK experiments in September 1985 and October 1986, respectively, at the Army Corps of Engineers Field Research Facility (FRF) in Duck, N.C. The DUCK85 experiment (Mason, et al. 1987) was used to perform initial testing primarily with standard 35 mm cameras and simple photographic time exposure techniques. The images acquired were projected onto an x-y digitizer table and the location of the intensity maximum determined visually (Holman and Lippmann 1987). Results from that experiment were encouraging, but indicated a need for further quantification and more sophisticated digitization methods.

37. During SUPERDUCK the use of video imagery was implemented as an improvement to the photographic technique. A Panasonic black-and-white television camera was mounted on top of a 40 m high tower erected on the dune crest. Figure 8 is a map of the field site during the October portion of the SUPERDUCK experiment showing the location of the study area, referred to as the minigrid, in relation to the FRF tower and the ground coverage associated with the camera.

38. Hourly video records of twenty minute length were acquired from October 6-16. Time exposures were created digitally by mathematically averaging successive video frames over a ten minute period using an Imaging Technology image processing system in a DEC LSI 11/73 host computer (Figure 1 (b) is an example time exposure image from October 10). Using the photogrammetry results, the time exposure image can then be rectified to produce a map view with correct scaling. The rectification process involves mapping the oblique image intensities, pixel by pixel, onto the scaled grid. From the rectified view, cross-shore intensity profiles at prescribed long-shore distances are easily found. Figure 9 is the rectified image of the minigrid area outlined in Figure 1 (b). Figure 10 shows an example cross-shore intensity profile and the local bathymetry. Clearly, there are local maxima in the intensity distribution in the vicinity of the shoreline and the bar. Note that the intensity values are non-dimensional numbers whose magnitude is not related to the bathymetry.

39. The use of the image processing system has many advantages. Extracting information in this manner allows for minimum handling of raw data and

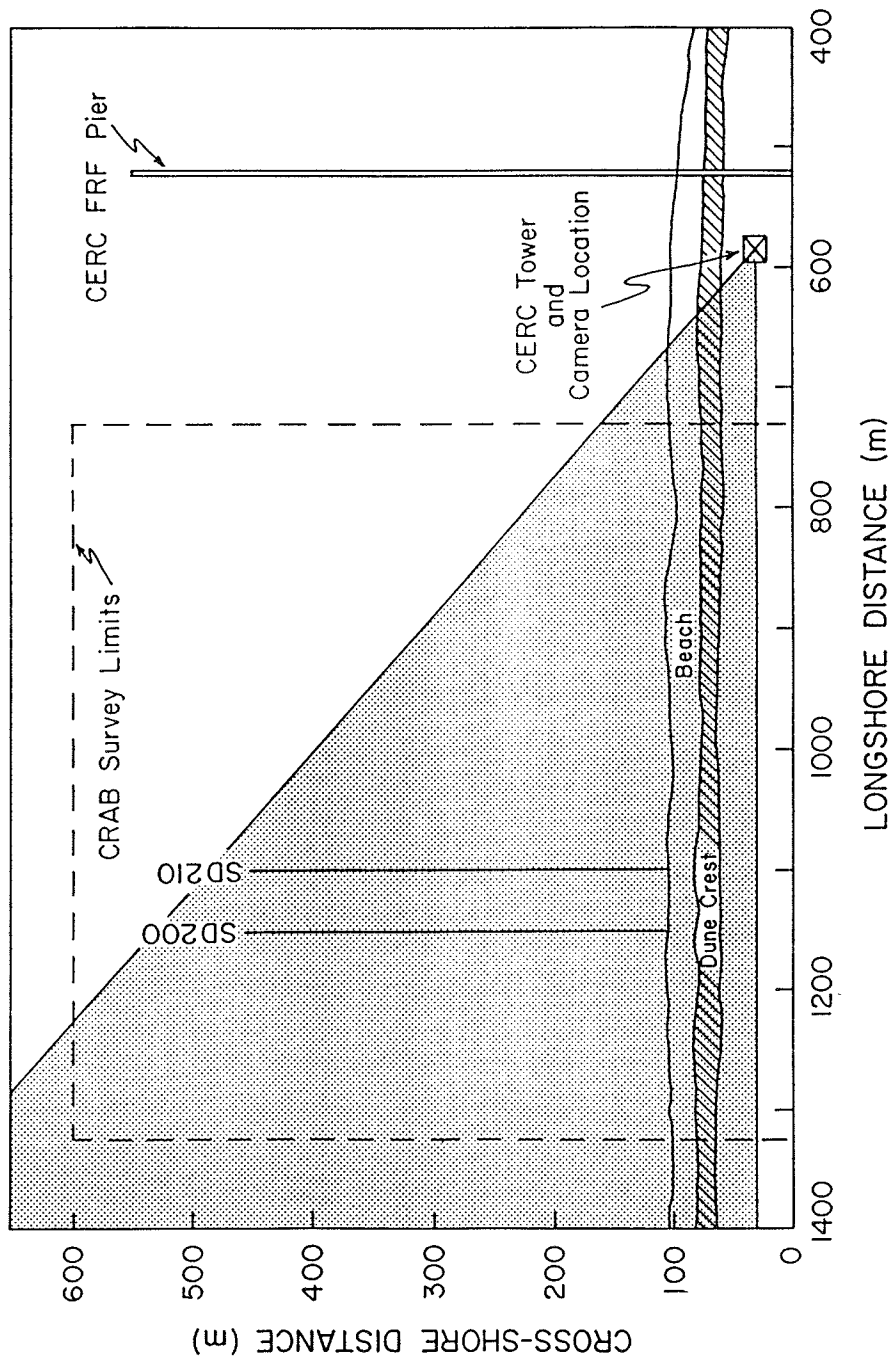


Figure 8. Map of the field site during the October portion of SUPERDUCK. The stippled area indicates the ground coverage in the field of view of the camera. Cross-shore transect SD200 is the location of some example profiles in the text while SD210 is the location closest to the main instrument line in SUPERDUCK. Longshore spacing in the CRAB survey was 20 min (there exists an intermediate line, SD205).

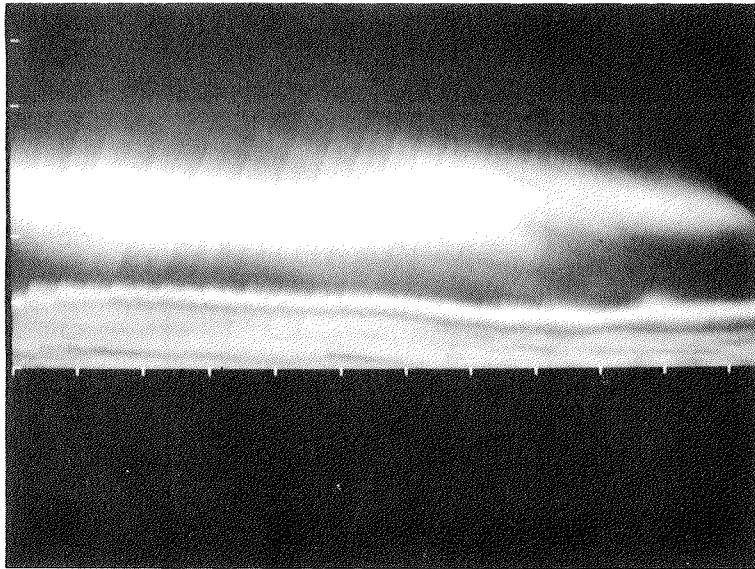


Figure 9. Rectified time exposure image obtained at low tide on October 16, 1986 encompassing the minigrad area. The longshore and cross-shore distances are scaled equally with tickmark spacing of 50 m. The thin white band indicates the shore break while the broader offshore band shows breaking over the bar. The relative size in raster width reflects the pixel resolution in the original time exposure.

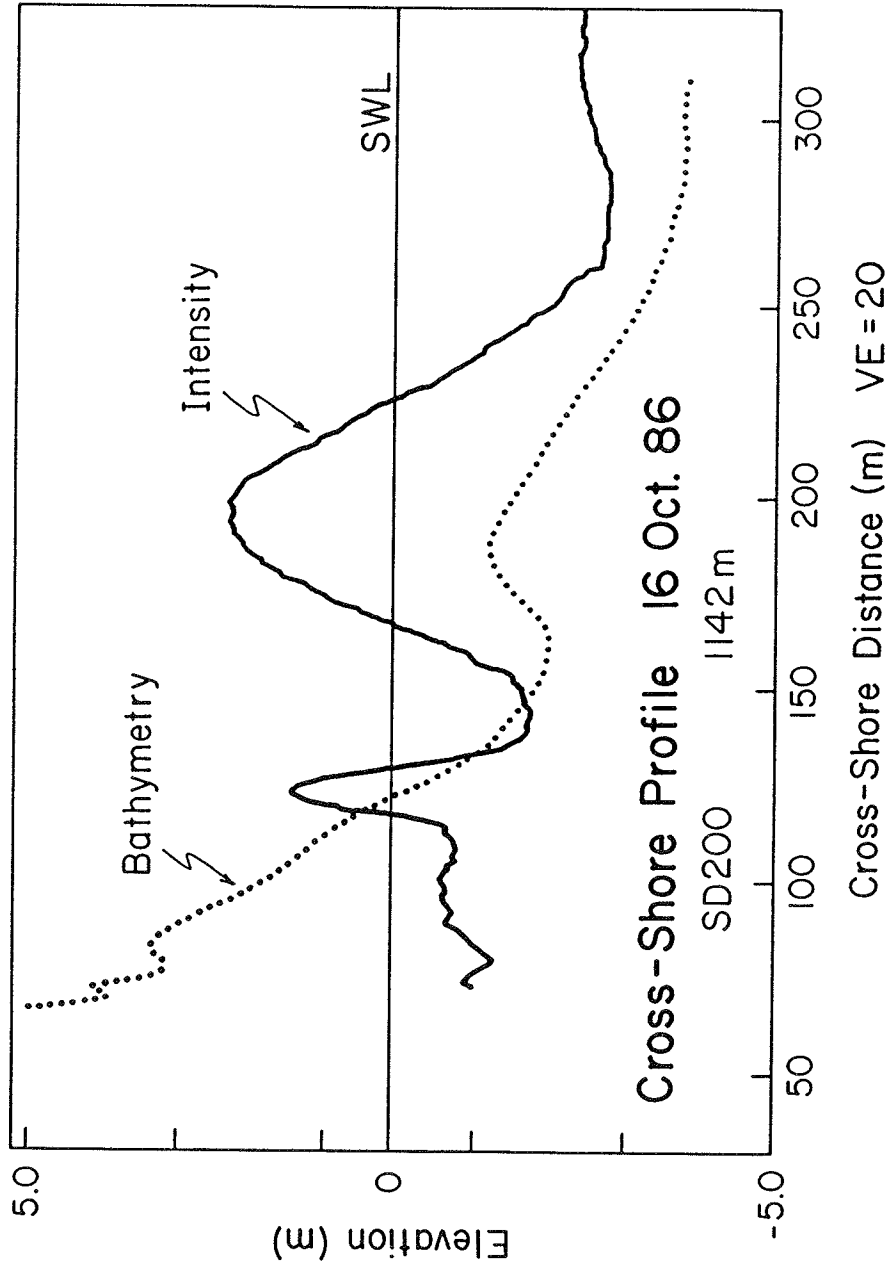


Figure 10. Example cross-shore intensity profile and bathymetry for October 16, 1986 during SUPERDUCK. The vertical intensity values are non-dimensional with magnitudes that are not related to the bathymetry

reduces any personal bias associated with visual image analysis. Furthermore, with the aid of the image processor we may digitally enhance the images to best reveal the information available. For example, though some video records do not yield high contrast raw images, the image processor allows us to increase the dynamic range of the image by stretching the contrast to as many as 256 gray shades.

40. Ground truth bathymetry data during SUPERDUCK was collected by the FRF staff using the CERC Coastal Research Amphibious Buggy (CRAB) (Birkmeier and Mason 1984). Figure 8 shows the location of the intensive survey region. Bathymetric data were collected daily (October 6, 9-16) along preset cross-shore profile lines spaced approximately 20 m apart alongshore. Each survey went beyond the first (and most prominent) sand bar, with the exception of the 10th when extreme wave conditions prevented survey completion. Figure 11 shows three-dimensional oblique views of the minigrid survey for October 6, 9, 11, 13, 15, and 16.

41. A maximum of 20 shore-normal profiles within the minigrid area were analyzed for each data run. As in Figure 9, each profile contained a maximum intensity (or peak) in the vicinity of the shoreline and the bar, provided the waves were breaking offshore. Given the large amount of data (464 cross-shore comparisons) not all profile plots are included. Instead most of the data is summarized in the following analysis using two-dimensional plan-view maps indicating the surveyed bar location and digitized intensity maximum location at different stages of the tide. With this sampling scheme we are able to determine the behavior of the cross-shore intensity distribution in relation to the bathymetry under varying wave conditions, water levels, and beach state. Table 1 summarizes the sampling times, wave conditions, and video quality for each data run.

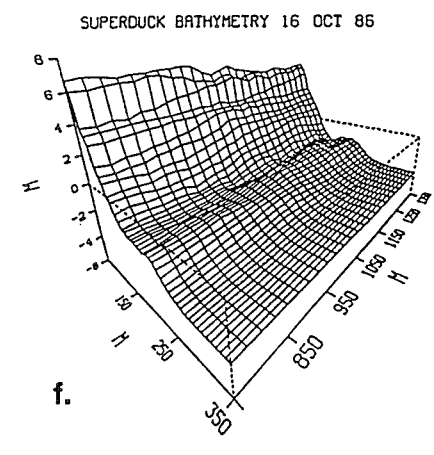
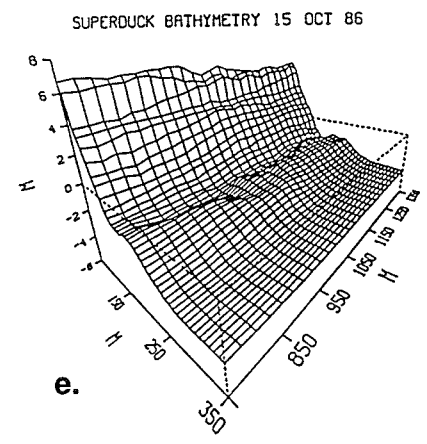
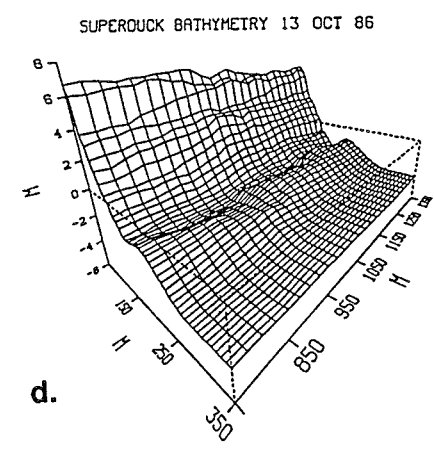
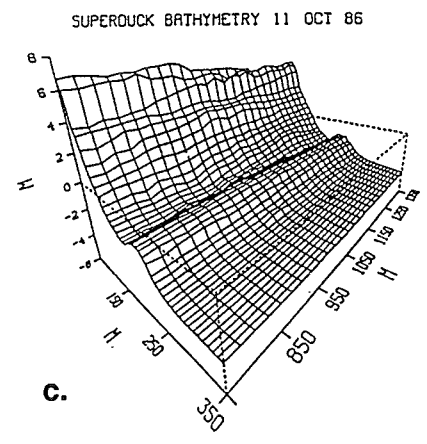
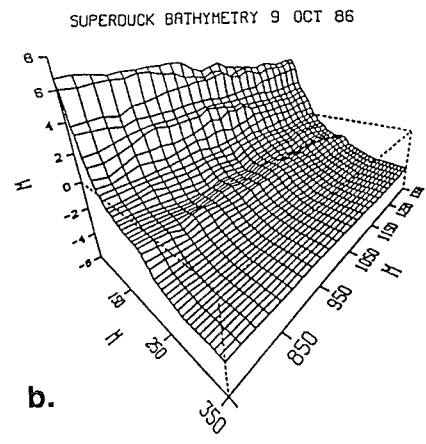
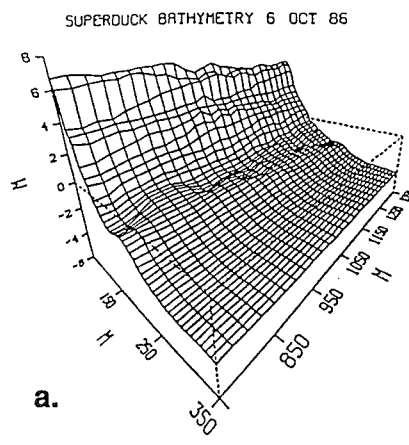


Figure 11. Three-dimensional oblique views of the minigrd survey during SUPERDUCK. (Courtesy Bill Birkemeier and the FRF)

Table 1
Sampling Time, Wave Conditions and Video Quality Images
Discussed in the Text

Date	Tide (m)		Time	Hrms (m)	f (Hz)	Video Quality
06	low	-0.11	1400 EST	0.82	0.1680	good
06	mid	0.25	1730 EST	0.56	0.1719	good
09	high	0.80	1130 EST	0.43	0.1641	good
09	mid	0.27	1445 EST	0.44	0.1641	good
09	low	-0.27	1800 EST	0.38	0.1641	good
10	low	-0.08	0600 EST	0.33	0.2656	good
10	mid	0.55	0915 EST	1.35	0.1484	poor (rain)
10	high	1.10	1230 EST	1.58	0.1406	poor (rain)
11	low	0.09	0720 EST	2.06	0.1094	good
11	mid	0.56	1040 EST	2.13	0.1563	good
11	high	1.06	1400 EST	2.06	0.1016	good
12	low	0.03	0830 EST	1.65	0.0938	excellent
12	mid	0.45	1145 EST	1.85	0.0859	excellent
12	high	0.93	1500 EST	1.77	0.0859	excellent
13	low	-0.22	1000 EST	1.20	0.0820	good
13	mid	0.15	1230 EST	1.25	0.0977	good
13	high	0.73	1600 EST	1.25	0.0977	good
14	low	-0.36	1100 EST	0.75	0.0977	poor (noisy)
14	mid	0.17	1400 EST	0.69	0.1055	poor (noisy)
14	high	0.70	1700 EST	0.61	0.0938	poor (noisy)
15	low	-0.22	1130 EST	0.77	0.1719	good
15	mid	0.30	1445 EST	0.64	0.1719	good
15	high	0.76	1800 EST	0.54	0.1641	good
16	high	0.91	0600 EST	0.49	0.2349	good
16	mid	0.40	0915 EST	0.68	0.1992	good
16	low	-0.30	1230 EST	0.72	0.2031	good

PART V: RESULTS

Time Exposures

42. The research objectives of the time exposure technique are three-fold. The first is to detect the presence of a sand bar by an offshore intensity maximum. The second is to determine the cross-shore length scale of the bar from the location of the intensity maximum. The third is to detect the presence of any longshore variability in the bar and determine appropriate longshore length scales. We will examine each objective in turn.

43. The theoretical dissipation model suggests that our best results will be obtained for small waves that just break over the bar (H_c^* values of 0.5 to 1.0). For October 6th, an average value of H_c^* was approximately 0.85, and while the bathymetry was complex, there were local regions of good bar definition (Figure 11a). Figure 12 shows the mid-tide intensity transects for the three best-defined sand bar profiles (determined from minigrid bathymetry). The intensity maxima clearly indicate the presence of the sand bar although the peak definition is somewhat subtle for the $y=1187$ transect, consistent with the subtle nature of the bar. There is excellent agreement between the locations of the intensity maxima and bar crest, well within the resolution of the image. This supports the validity of the model and the potential of the technique for imaging morphology under optimal conditions.

44. Figure 13 is the rectified time exposure image obtained at low tide on the 11th, a day when model performance was expected theoretically to be poorer due to the larger wave heights (average $H_c^* = 4.3, 2.6,$ and 2.4 for low, mid and high tide, respectively). The bathymetry survey (Figure 11c) showed the bar to be linear with no longshore variability. The intensity distribution in Figure 13 confirms this, showing a clear linear pattern and providing a good qualitative description of the sand bar.

45. While the qualitative description is good, the quantitative behavior of the model breaks down in an unexpected way. Figure 14 shows the location of the intensity peak for low, mid, and high tide over the minigrid area. Also shown are the locations of the mean shoreline and bar crest. The latter is depicted by a central line (the best estimate of bar crest position) surrounded by a stippled area, reflecting the fact that the bar itself may not be well defined. (From Figure 12, it is clear that bar definition is typically

October 6 Time Exposure

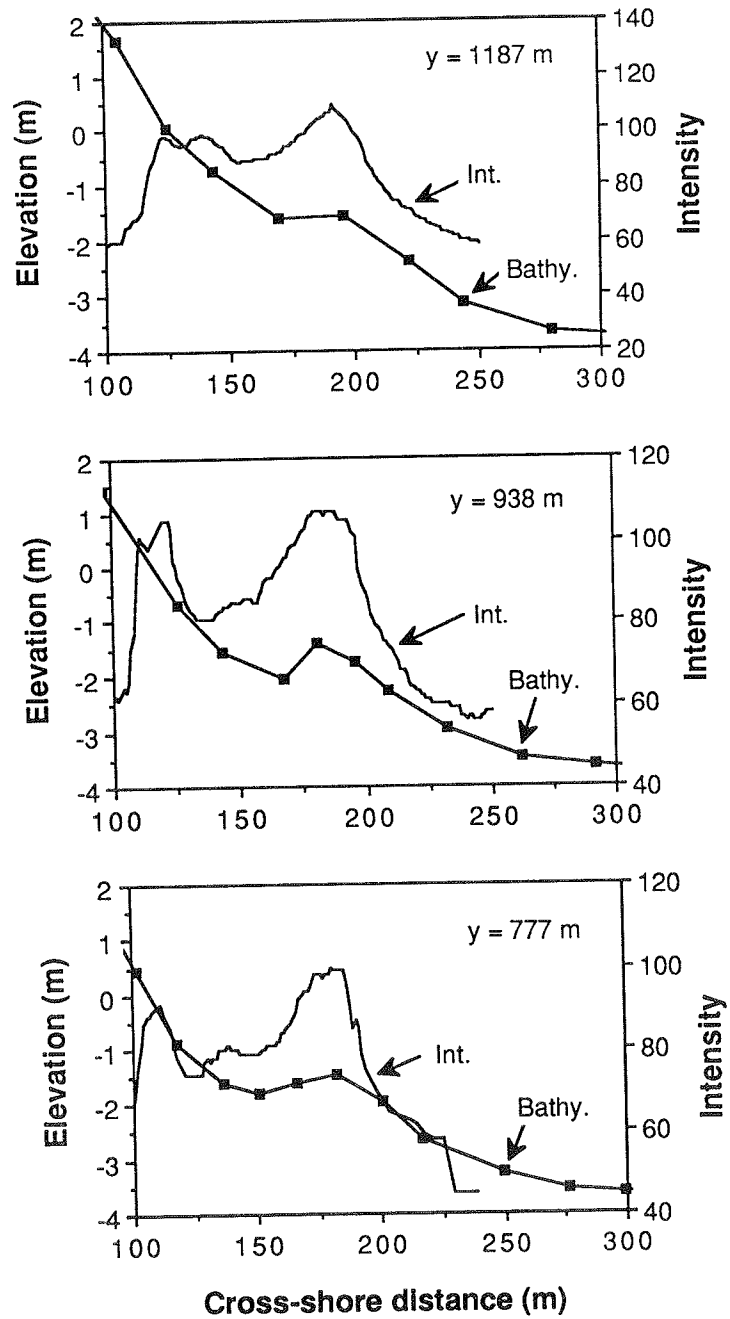


Figure 12. Bathymetry and cross-shore intensity profiles from a simple time exposure obtained at mid tide on October 6, 1986. The three transects were chosen as having the best-defined bars.

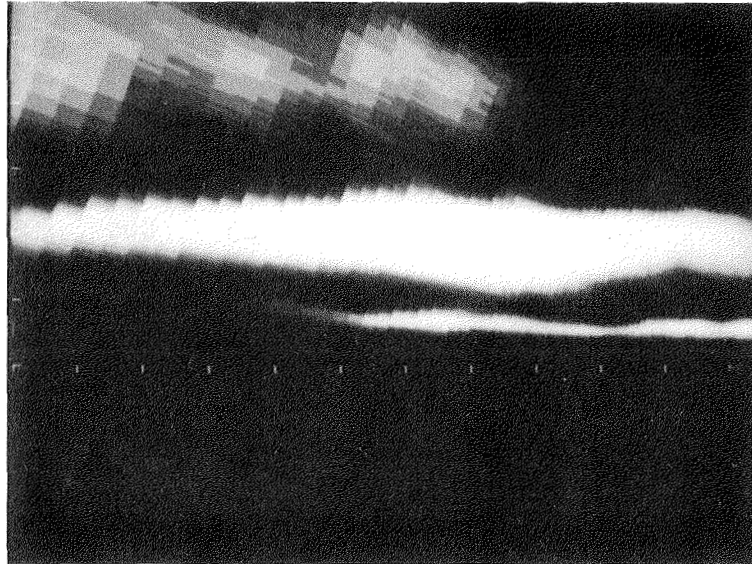


Figure 13. Rectified time exposure image encompassing the minigrid area obtained at low tide on October 11, 1986. The longshore and cross-shore distances are scaled equally with ticmark spacing of 50 m. The image contrast has been stretched to better reveal the bar location. The weak offshore intensity maximum corresponds to a poorly-defined second bar.

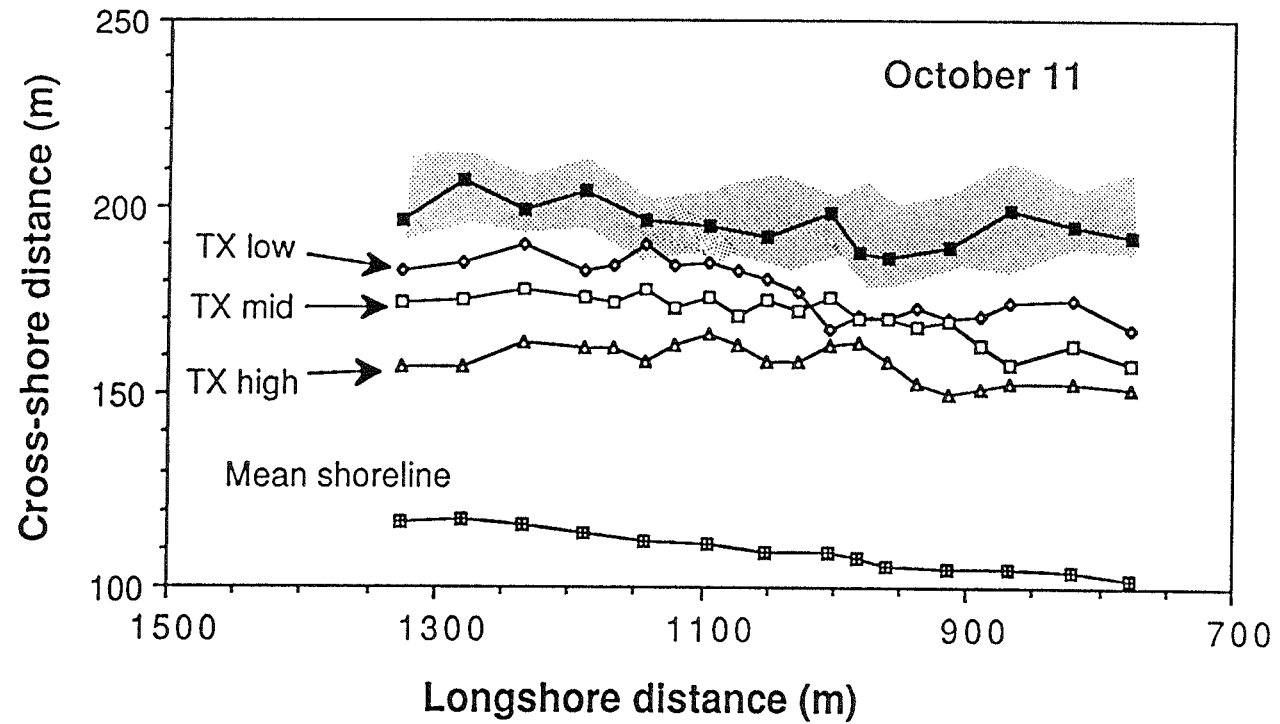


Figure 14. Location of the mean shoreline, measured bar crest, and intensity maxima from simple time exposures (tx) obtained at low, mid, and high tide on October 11, 1986. The stippled area indicated the area around the crest for which the water depth is within 5 percent of h_c .

based on three CRAB survey points with a typical spacing of 15 m and whose locations are subject to operator subjectivity. To parameterize this uncertainty we have added the stippled area whose bounds correspond to a deepening by 5 percent of the bar crest depth, h_c , usually 5-10 cm).

46. The shape and trend of the bar in Figure 14 appears to be preserved at all stages of the tide. However, the offshore location of the intensity peaks does not fall over the bar, and in fact lies inside the crest well into the trough. This result cannot be reproduced in any way by our model and shows that our assumption that the average visual wave breaking signal represents incident wave dissipation is invalid under these conditions.

47. Investigation of the original video images reveals two apparent sources for the error. The finite distance required for wave reformation after passing the bar crest appears to provide a minor landward offset. However, most of the error appears to stem from preferential persistence of foam in the trough region. This differential in foam persistence weights the intensity maximum shoreward from the location of maximum wave dissipation. We know of no testable physics to describe this behavior and hence allow us to remove the bias. By examining those records for which a well-defined bar is present, we find that approximately 42 percent of the intensity maxima were located shoreward of the bar crest and that these were generally associated with high waves and strong onshore winds. This latter observation suggests a potential mechanism which would need considerable further testing.

48. The capabilities of the technique for detecting and quantifying longshore variability are illustrated in Figure 15, a comparison of shore-parallel transects of intensity and bathymetry for October 16th, a day of lower waves ($H_c^* = 1.7$). The two transects differ by 10 m in offshore location and are centered about the mean bar position. The intensity and bathymetry profiles for this day and for all others tested from SUPERDUCK showed similar structure. The presence of topographically-trapped rip currents, originally a concern, does not appear to cause a problem since the relative "darkness" of the rip is imaged in a consistent manner with the "darkness" due to reduced breaking over the underlying channel. Several other examples of rhythmic morphology from other times of year confirm the robustness of the technique for this purpose, indicating that the time exposures can in fact be used to detect and measure dominant longshore length scales of a sand bar system.

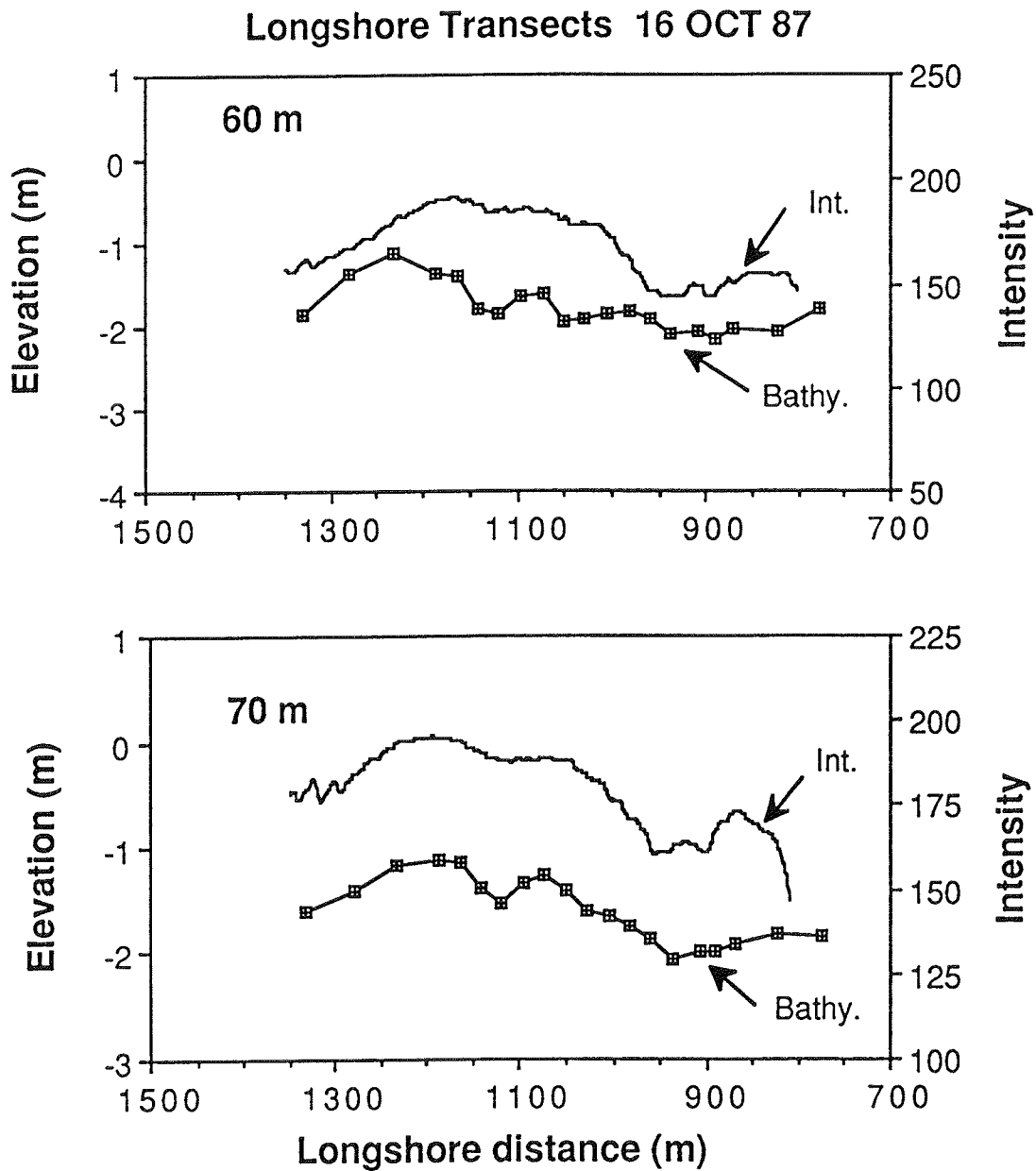


Figure 15. Shore-parallel transects centered over the mean bar distance, 60 m (upper panel) and 70 m (lower panel) offshore, from a simple time exposure obtained at low tide on October 16, 1986. Variations of intensity correspond to the underlying bathymetry

49. Overall, the time exposure technique appears to be a very useful tool for determining the presence of a bar system as well as the presence and length scales of longshore variability. Cross-shore scales are well reproduced under certain conditions, but an observer hoping to use photographic time exposures, for example, would have to bear in mind the potential foam bias and make a qualitative assessment of the problem before quantifying any sample (residual foam is visible, so at least an assessment can be made). This problem seems to reduce the effectiveness of the time exposures. However, if an image processing system is available, more powerful techniques are available to improve the situation. We have developed one technique, called differencing time exposure, that accomplishes our purposes.

Differencing Time Exposures

50. One way to altogether avoid the dynamics of residual foam accumulation is to eliminate unwanted, persistent signals that do not pertain to active breaking (thus energy dissipation). This elimination can be accomplished by subtracting video frames, separated in time by a given interval (commonly 0.5 - 1.0 seconds), to yield a difference image. Regions of little or no contrast change, such as areas of persistent foam, will show zero difference. Areas of active breaking will show large intensity changes, hence large difference signals. A time exposure can be made by averaging a set of these difference images over a suitable period, again ten minutes for our case. Figure 16 is an example differencing time exposure image from October 11. The offshore breaking pattern is indicated again by the high intensity band offshore.

51. The differencing technique requires the selection of two free parameters to yield an optimal image. The first is the time interval between images for image subtraction, mentioned above. The second is a threshold value below which contrast differences are considered negligible (and are mapped to zero). This threshold serves the double purpose of eliminating minor values of difference that result from camera shake or the inevitable video noise, as well as eliminating the negative values of difference (since time averaging allowing both positive and negative differences must always give a result of zero). While resulting image quality is influenced by the

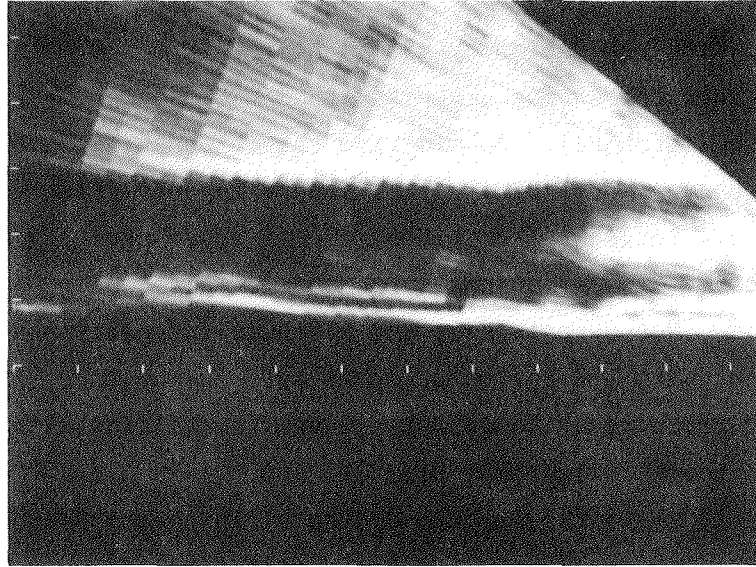


Figure 16. Rectified differencing time exposure obtained at low tide on October 12, 1986. The bright white bank offshore indicates the presence of a sandbar, whereas the shoreline is indicated by a relative darkness within the shorebreak region. The longshore and cross-shore distances are scaled equally with ticmark spacing of 50 m.

particular values of these parameters, the conclusions about sand bar morphology (intensity peak locations) are not overly sensitive. Fixed values have been used throughout this paper to eliminate selective bias.

52. Examination of the differencing time exposure technique begins by looking at the limiting case where waves just begin to break over well-defined bar crests. Figure 17 is a bar location map for October 9th indicating the estimated bar location and intensity maxima at low ($H_c^* = 0.8$) and mid tide ($H_c^* = 0.6$) for the differencing algorithm ($H_c^* = 0.45$ at high tide and no waves were breaking offshore). At mid tide the intensity maximum location falls within the survey error of the position of the bar crest, indicating a good estimate at all longshore locations. Cross-shore profiles corresponding to several regions with well-defined bar crests (indicated in Figure 17) are shown in Figure 18. Not surprisingly the offshore intensity maximum shows excellent agreement with the bar crest location. Furthermore, the intensity maximum has moved offshore at lower water level, consistent with the results of the dissipation model (Figure 6; equation 10).

53. Figure 19 shows the results of the differencing technique for October 11 when the bar was linear but the simple time exposure results were their worst. The improvement is immediately evident; at high tide ($H_c^* = 2.4$) the intensity locations lie quite near the crest within the range of bar estimate for most of the data. At lower tide levels the intensity moved offshore consistent with greater dissipation offshore. For low tide ($H_c^* = 4.3$) the mean value of $\Delta x/x_b \approx 39\%$, somewhat above the same range for the theory (Figure 6) but not unreasonable.

54. Figure 20 shows the performance of the technique for October 16th when the bathymetry was quite variable in the longshore. At high tide ($H_c^* \approx 0.4$), the waves were barely breaking over the bar and the intensity maximum provided an excellent mapping of even this complicated bar morphology. However, for low tide ($H_c^* \approx 1.7$), the differencing time exposure maximum is further offshore and corresponds to the location of the more continuous slope break at about 1.75 m depth. The H_c^* value for the slope break was approximately 1.0, large enough to allow significant breaking. This may explain the "selection" by the technique of the straighter slope break instead of the complicated and more poorly defined bar crest.

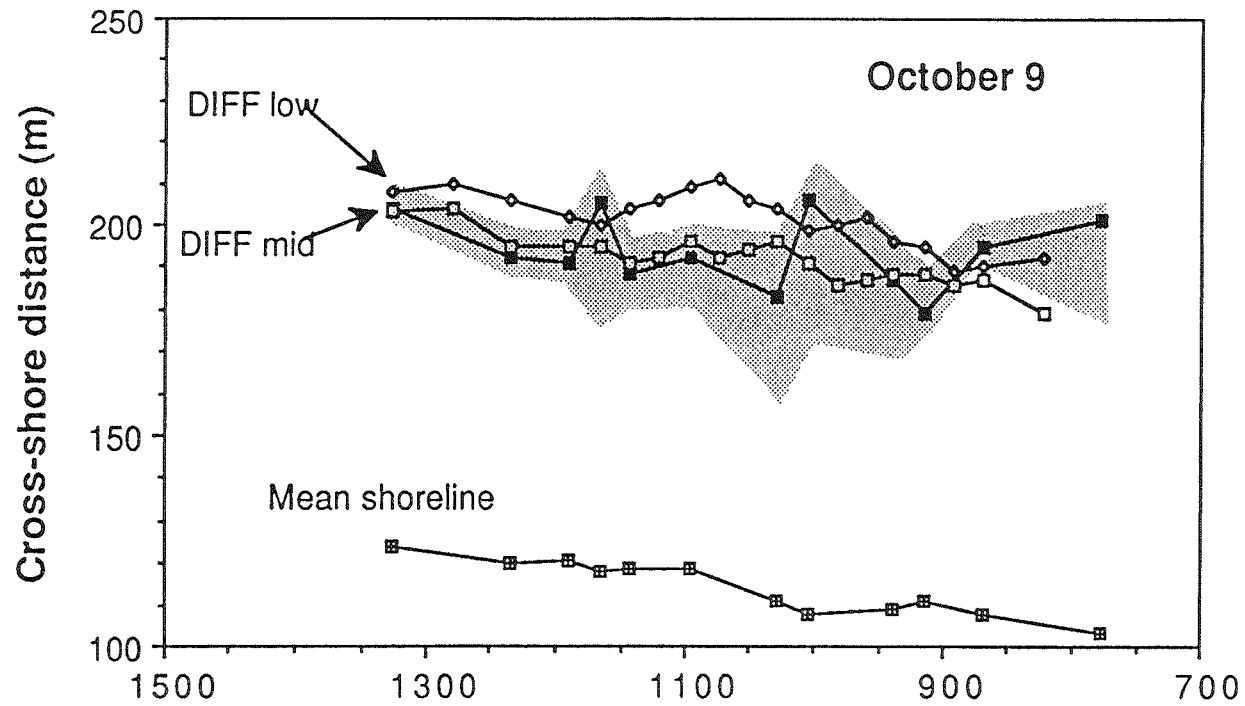


Figure 17. Location of mean shoreline, measured bar crest, and intensity maxima from differenced time exposures (diff) obtained at low and mid tide on October 9, 1986. The stippled area indicates the area around the crest for which the water depth is within 5 percent of h_c .

October 9 Differencing Time Exposure

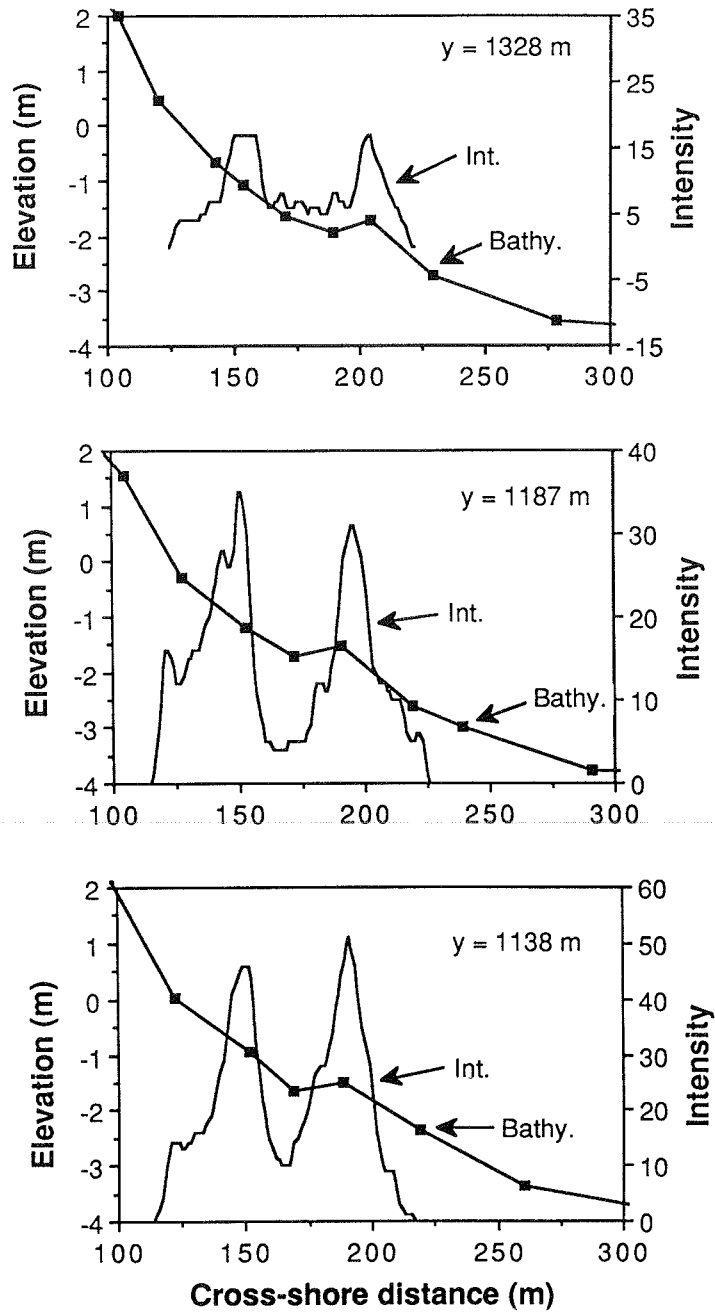


Figure 18. Local bathymetry and cross-shore intensity profiles from a differenced time exposure obtained at mid tide on October 9, 1986, for the three best-defined sand bar locations.

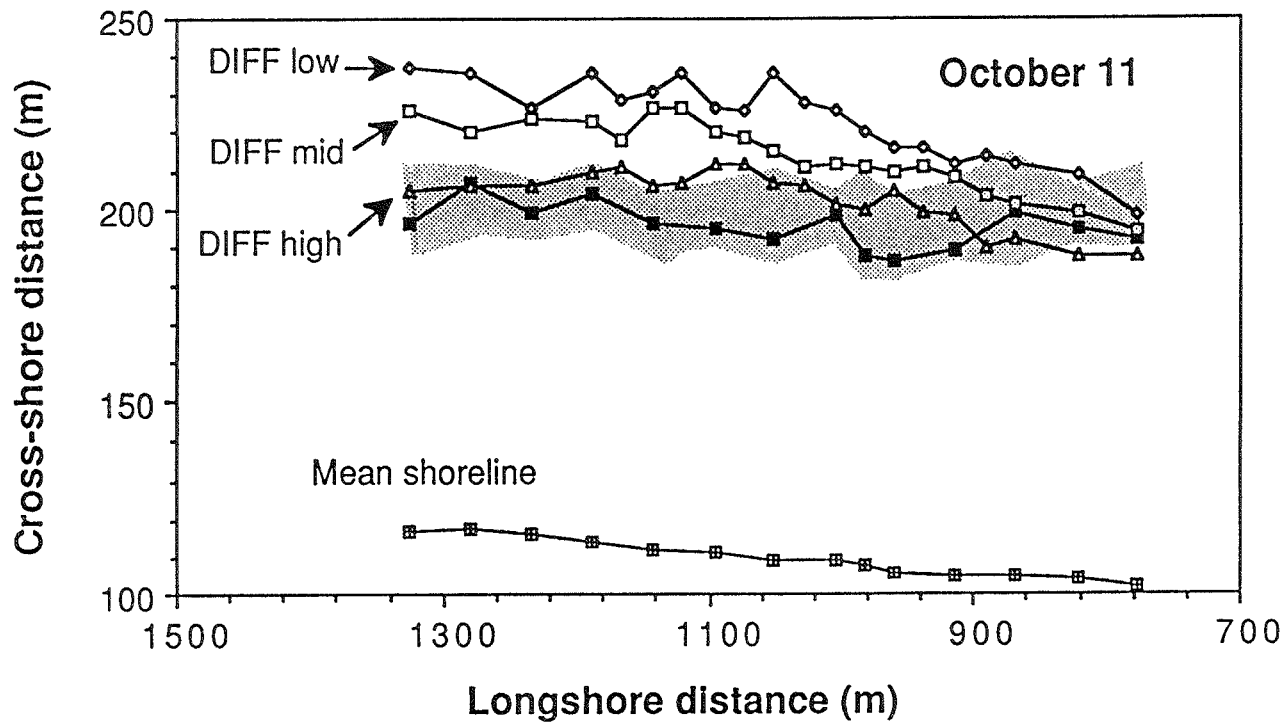


Figure 19. Location of mean shoreline, measured bar crest, and intensity maxima from differenced time exposures (diff) obtained at low, mid, and high tide on October 11, 1986. The stippled area indicates the area around the crest for which the water depth is within 5 percent of h_c .

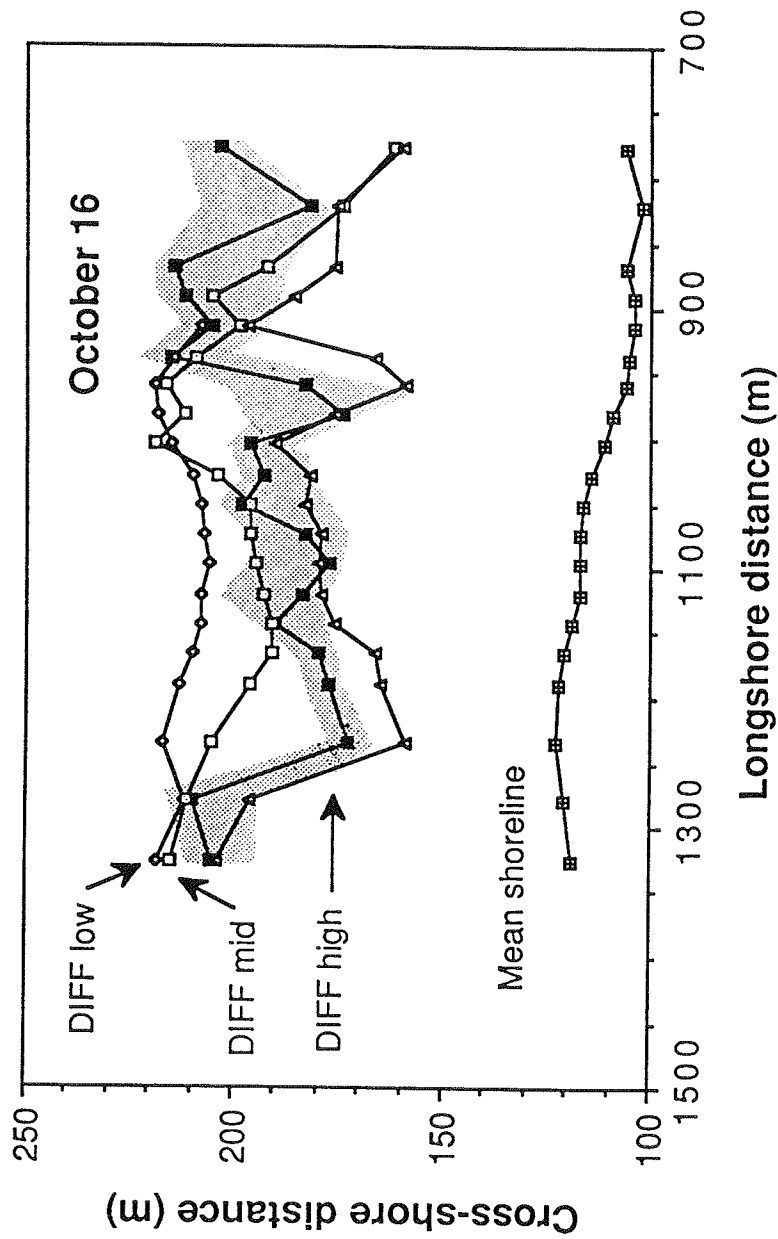


Figure 20. Location of mean shoreline, measured bar crest, and intensity maxima from differenced time exposures (Diff) obtained at low, mid, and high tide on October 16, 1986. The stippled area indicates the area around the crest for which the water depth is within 5 percent of h_c .

55. The above discussion supports the hypothesis that our time exposure technique (modified by a differencing algorithm) is representative of energy dissipation of incident wave breaking. Continuing the comparison, we attempt to characterize the discrepancies in bar location, Δx , as a function of non-dimensional wave height, H_c^* . The Δx values arising in the differencing technique for October 9, 11-16 are normalized by the mean distance to the bar crest (different along each profile for each day) and plotted against H_c^* in Figure 21. Despite the greater noise in the field observations, the results are similar to the model behavior shown in Figure 6, again supporting the validity of the model.

Shoreline Agreement

56. A further feature in time exposures is a shore break which shows up as higher intensity values along the beach face. The cross-shore profiles shown in Figures 12 and 18 have well-defined peaks in the vicinity of the shoreline. This intensity maxima for all cross-shore profiles (from simple time exposures) are compared quantitatively with the calculated shoreline location in Figure 22. The correlation is very good ($r = 0.92$), however, the slope of the line through the data is slightly positive, a result of swash dynamics for which we have no model. For individual days, the agreement is excellent; for example, on the 12th when image quality was best the intercept is -2.0 and the slope 1.02 ($r = 0.97$).

57. The persistence of foam near the mean run-up location generates an unusual result for the differencing technique. Since foam intensity appears fairly constant, contrast difference will always be low, the mean shoreline for the differencing image often shows an intensity minimum that corresponds to the location of the maximum for the simple time exposure. However, shoreline location appears best done with the simple time exposure.

Differencing Time Exposure Data

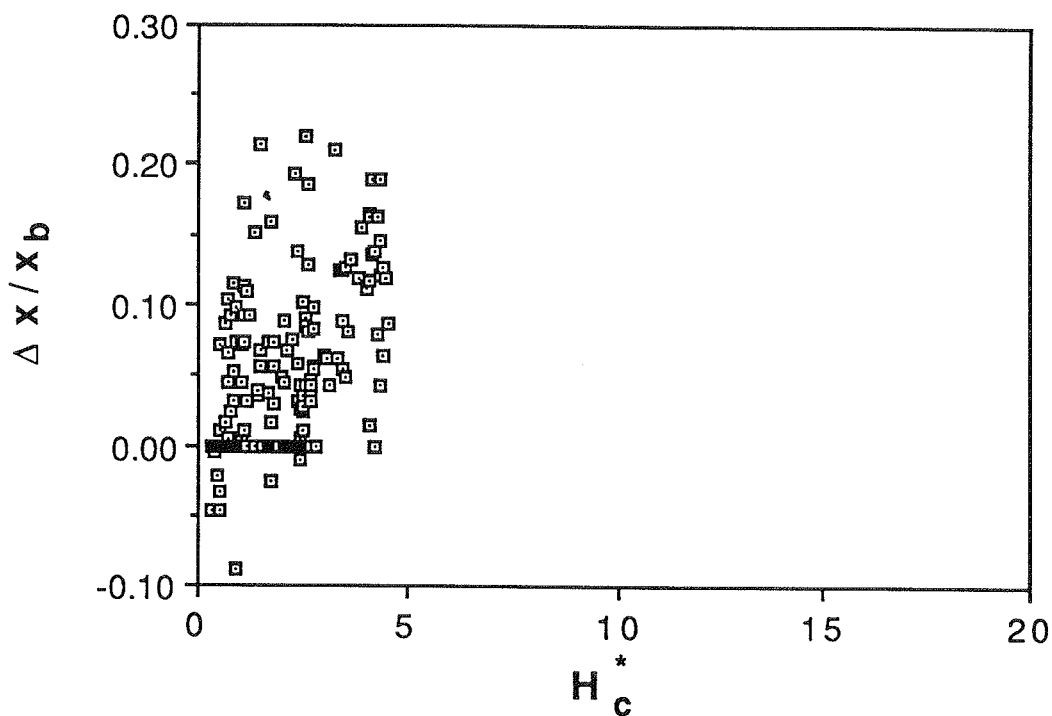


Figure 21. Results from differencing time exposures on October 9, 11-13, 15-16 showing the fractional error in locating the bar crest plotted against non-dimensional wave height, H_c^* . Negative $\Delta x / x_b$ values indicate a landward offset in intensity bar location estimate.

Shoreline Agreement

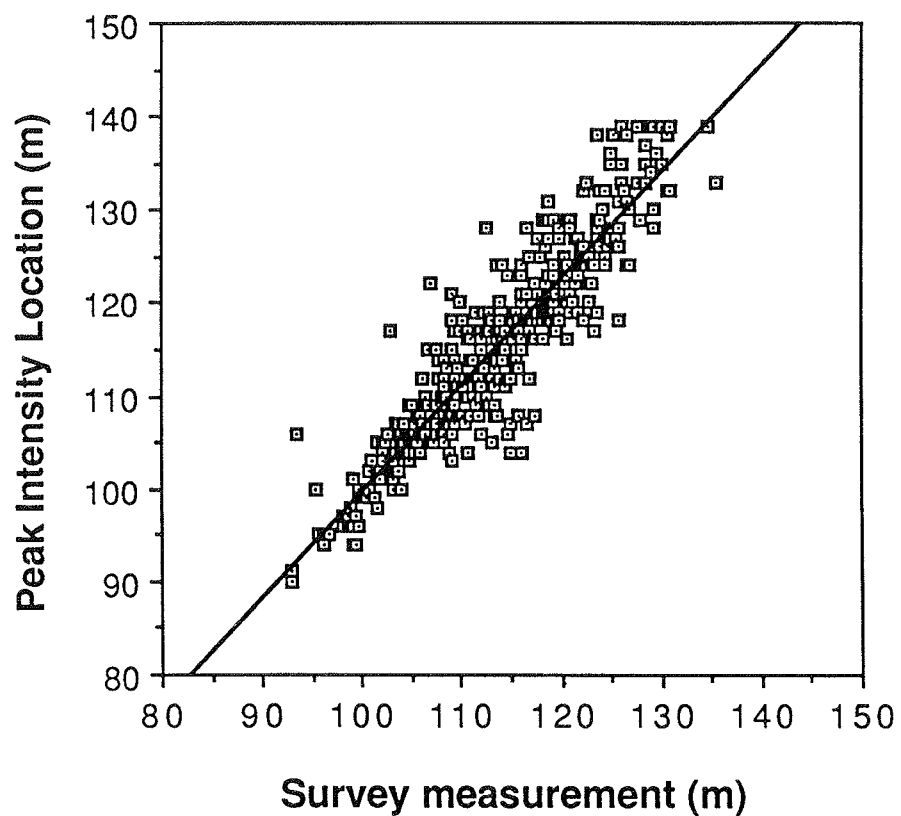


Figure 22. All shoreline intensity maxima locations from simple time exposures obtained at low, mid, and high tide on October 6, 9-16 plotted against measured shoreline location. The regression line is given by $y = -14.8 + 1.15x$ ($r = 0.92$).

PART VI: DISCUSSION

58. Both the simple time exposure and the differencing time exposure techniques seem to provide a valuable tool for studying nearshore morphology. Both detect the presence of a bar system and allow measurement of any dominant longshore length scales of rhythmicity. Both can be used to estimate cross-shore length scales, a necessary pre-requisite for testing bar generation models. The differencing technique is based on sound physics, so errors are understood and, fortunately, are constrained by incident wave saturation. For the simple time exposure technique, the physics becomes confused by problems with residual foam, so that, for non-dimensional wave heights (H_c^*) greater than about 1, estimates of bar position can be subject to error for which we have no model. Nonetheless, our results show that the simple time exposure will generally yield better bar position estimate, provided the user is aware of the residual foam problem. This is due to a fortuitous case of compensating errors; dissipation of larger waves tends to give errors in the offshore direction while foam tends to compensate toward the onshore. Unfortunately, we have only a qualitative understanding of the process.

59. The successful parameterization of the differencing technique by the non-dimensional wave height, $H_c^* = H_{rms}/\gamma h_c$, is reassuring from a theoretical point of view. However, it is of dubious practical value since we do not know h_c , the depth at the bar crest. Instead, a user of the technique must refer back to the qualitative wave parameterizations. Both simple and differencing techniques work well when the waves are "just breaking" over the bar. The simple technique starts to break down when the presence of foam no longer seems directly related to the amount of local dissipation. Both of these limits are of a type that can be visually assessed by an intelligent user.

60. The calibration of the time exposure technique discussed in this paper assumes that the appropriate measure of a sand bar location is the point of minimum depth. This may not always be true. For example, for the bar generation mechanism presented by Holman and Bowen (1982) the sand bar is treated as a perturbation to an underlying beach profile. The point of maximum perturbation will always be offshore from the point of minimum depth, on the seaward slope of the typical bar where the local slope equals a representative mean slope. Thus the errors in the time exposure technique will probably be

less for this application. Holman and Bowen (1982) also point out that in their theory, a low-tide terrace can be thought of as a small amplitude bar. Again, the appropriate location of the maximum perturbation would be at the slope break, just the point imaged by the time exposure technique.

PART VII: CONCLUSIONS

61. We have developed a technique to measure the scales and morphology of natural sand bars based on the preferential dissipation of wind waves and swell over the shallows of the bar. This is imaged photographically, with statistical uncertainty reduced by the use of time exposures (averaging over a length of time long compared to modulation time scales for incident wave height). Analysis of the photogrammetry shows that positional information in the resulting images can be quantified to an accuracy of 5 percent of the distance to the camera.

62. Theoretical modelling shows the sensitivity of incident wave dissipation to perturbations in bottom slope, hence the potential for using dissipation to locate bars. An important parameter is the non-dimensional wave height, $H_c^* = H_0/\gamma h_c$. For $H_c^* = 0.5 - 1.0$, the waves are just breaking and the dissipation maximum corresponds well to the bar crest position. Larger H_c^* values result in weighting the dissipation maximum farther offshore up to a maximum location beyond which the local wave field is saturated. The maximum discrepancies based on a reasonable example are 35 percent of the true bar crest distance.

63. Ground truth testing, conducted during SUPERDUCK, confirm the capabilities of the time exposure technique for detecting the presence of a sand bar system as well as detecting longshore variability and rhythmicity and quantifying length scales. Cross-shore scale estimates are accurate for small H_c^* , but for higher waves persistent foam biases the intensity shoreward in ways for which we have no theory. The use of video differencing (the subtraction of consecutive frames) removes residual foam from the image and results from differencing time exposures appear totally consistent with our theoretical dissipation modelling.

REFERENCES

- Battjes, J.A., Set-up due to irregular waves, in Proceedings of the 13th Conference on Coastal Engineering, 1993-2004, American Society of Civil Engineers, New York, 1972.
- Battjes, J. A. and J. P. F. M. Janssen, Energy loss and set-up due to breaking of random waves, in Proceedings of the 16th Conference on Coastal Engineering, p. 569, American Society of Civil Engineers, New York, 1978.
- Birkemeier, W. A. and C. Mason, The CRAB: a unique nearshore surveying vehicle, J. Surv. Eng., 110(1), 1-7, American Society of Civil Engineers, New York, 1978.
- Bowen, A. J., Simple models of nearshore sedimentation: beach profiles and longshore bars, in S.B. McCann (Editor), Coastline of Canada, Littoral Processes and Shore Morphology, Geol. Surv. Can., Pap., 80-10, 1-11, 1980.
- Bowen, A. J. and D. L. Inman, Edge waves and crescentic bars, J. Geophys. Res., 76, 8662-8671, 1971.
- Carter, T. G., Liu, P. L. and C. C. Mei, Mass transport by waves and offshore sand bedforms, J. Waterways, Harbors, Coastal Engineering Division, 165-184, American Society of Civil Engineers, New York, 1973.
- Collins J. I., Probabilities of breaking wave characteristics, in Proceedings of the 13th Conference on Coastal Engineering, 399-412, American Society of Civil Engineers, New York, 1970.
- Crowson, R. A., Birkemeier, W. A., Klein, H. M. and H. C. Miller, SUPERDUCK nearshore processes experiment: summary of studies, CERC Field Research Facility, Technical Paper, US Army Engineer Waterways Experiment Station, Vicksburg, MS, in press.
- Galvin, C. J., Jr., and P. S. Eagleson, Experimental study of longshore currents on a plane beach, Tech. Memo. 10, U.S. Army Coastal Eng. Res. Center, Fort Belvoir, Va., 1965.
- Goda, Y., Irregular wave deformation in the surf zone, Coast. Eng. Jpn., 18, 13-26, 1975.
- Holman, R. A. and A. J. Bowen, Bars, bumps, and holes: models for the generation of complex beach topography, J. Geophys. Res., 87, 457-468, 1982.
- Holman, R. A. and R. T. Guza, Measuring run-up on a natural beach, Coastal Eng., 8, 129-140, 1984.
- Holman, R. A. and T. C. Lippmann, 1987. Remote sensing of nearshore bar systems - making morphology visible, Proceedings of the 20th Conference on Coastal Engineering, 929-944, American Society of Coastal Engineers, New York, 1987.

Holman, R. A. and A. H. Sallenger, Jr., Set-up and swash on a natural beach, *J. Geophys. Res.*, 87, 483-491, 1985.

Hwang, L.-S. and D. Divoky, Breaking wave set-up and decay on gentle slopes, in *Proceedings of the 12th Conference on Coastal Engineering*, 377-389, American Society of Coastal Engineers, New York, 1970.

Huntley, D. A., Guza, R. T. and E. B. Thornton, Field observations of surf beat, 1, Progressive edge waves, *J. Geophys. Res.*, 86, 6451-6466, 1981.

Keulegan, G. H., An Experimental study of submarine sand bars, U.S. Army Corps of Engineers, Beach Erosion Board, Tech. Memo., 3, 40 pp., 1948.

Kuo, C. T. and S. T. Kuo, Effect of wave breaking on statistical distribution of wave heights, *Proc. Civ. Eng. Oceans*, 3, 1211-1231, 1974.

Lau, J. and B. Travis, Slowly varying Stokes waves and submarine longshore bars, *J. Geophys. Res.*, 78, 4489-4497, 1973.

Mason, C., Birkemeier, W. A. and P. A. Howd, Overview of DUCK85 nearshore processes experiment, in *Proceedings of the 20th Conference on Coastal Engineering*, 818-833, American Society of Coastal Engineers, New York, 1987.

McCowan, J., On the solitary wave, *Philos. Mag., J. Sci.*, 32, 45-58, 1891.

Miller, R. L., Role of vortices in surf zone prediction: Sedimentation and wave forces, beach and nearshore sedimentation, *Spec. Publ. 24, Soc. of Econ. Paleontol. and Minerals*, Washington, D.C., 1976.

Oltman-Shay, J. and R. T. Guza, Infragravity edge wave observations on two California beaches, *J. Phys. Ocean.*, 17, 644-663, 1987.

Sallenger, A. H., Holman, R. A. and W. A. Birkemeier, Storm-induced response of a nearshore-bar system, *Mar. Geol.*, 64, 237-257, 1984.

Shepard, F. P., Longshore bars and troughs, U.S. Army Corps of Engineers, Beach Erosion Board, Tech. Memo, 15, 31 pp., 1950.

Short, A. D., Three dimensional beach-stage model, *J. Geol.*, 87, 553-571, 1975.

Stoker, J. J., *Water Waves*, Interscience, New York, 1957.

Thornton, E. B. and R. T. Guza, Energy saturation and phase speeds measured on a natural beach, *J. Geophys. Res.*, 87, 9499-9508, 1982.

Thornton, E. B. and R. T. Guza, Transformation of wave height distribution, *J. Geophys. Res.*, 88: 5925-5938, 1983.

Thornton, E. B. and R. T. Guza, Surf zone currents and random waves: Field data and models, *J. Phys. Ocean.*, 16: 1165-1178, 1986.